

C2D SPITZER-IRS SPECTRA OF DISKS AROUND T TAURI STARS: I. SILICATE EMISSION AND GRAIN GROWTH

JACQUELINE KESSLER-SILACCI¹, JEAN-CHARLES AUGEREAU^{2,3}, CORNELIS P. DULLEMOND⁴, VINCENT GEERS², FRED LAHUIS^{2,5},
NEAL J. EVANS, II¹, EWINE F. VAN DISHOECK², GEOFFREY A. BLAKE⁶, A. C. ADWIN BOOGERT⁷, JOANNA BROWN⁷, JES K.
JØRGENSEN⁸, CLAUDIA KNEZ¹, KLAUS M. PONTOPPIDAN²

Draft version October 29, 2018

ABSTRACT

Infrared $\sim 5\text{--}35\ \mu\text{m}$ spectra for 40 solar-mass T Tauri stars and 7 intermediate-mass Herbig Ae stars with circumstellar disks were obtained using the Spitzer Space Telescope as part of the c2d IRS survey. This work complements prior spectroscopic studies of silicate infrared emission from disks, which were focused on intermediate-mass stars, with observations of solar-mass stars limited primarily to the $10\ \mu\text{m}$ region. The observed 10 and $20\ \mu\text{m}$ silicate feature strengths/shapes are consistent with source-to-source variations in grain size. A large fraction of the features are weak and flat, consistent with μm -sized grains indicating fast grain growth (from $0.1\text{--}1.0\ \mu\text{m}$ in radius). In addition, approximately half of the T Tauri star spectra show crystalline silicate features near 28 and $33\ \mu\text{m}$ indicating significant processing when compared to interstellar grains. A few sources show large $10\text{--}20\ \mu\text{m}$ ratios and require even larger grains emitting at $20\ \mu\text{m}$ than at $10\ \mu\text{m}$. This size difference may arise from the difference in the depth into the disk probed by the two silicate emission bands in disks where dust settling has occurred. The $10\ \mu\text{m}$ feature strength vs. shape trend is not correlated with age or $H\alpha$ equivalent width, suggesting that some amount of turbulent mixing and regeneration of small grains is occurring. The strength vs. shape trend is related to spectral type, however, with M stars showing significantly flatter $10\ \mu\text{m}$ features (larger grain sizes) than A/B stars. The connection between spectral type and grain size is interpreted in terms of the variation in the silicate emission radius as a function of stellar luminosity, but could also be indicative of other spectral-type dependent factors (e.g. X-rays, UV radiation, stellar/disk winds, etc.).

Subject headings: circumstellar matter—stars:pre-main sequence—infrared: ISM: lines and bands—stars: formation—solar system: formation

1. INTRODUCTION

Dust in disks can be quite different from dust in the interstellar medium (ISM). Observations and chemical modeling (Grossman 1972, Gail 1998) suggest that the dust in the early stages of star formation is primarily composed of small ($<1\ \mu\text{m}$) amorphous silicates with strong features at approximately 9.7 and $18.5\ \mu\text{m}$ (for a summary, see Pollack 1984). Large modifications of the dust occur in the envelopes and disks around young stars, as the initially small grains are processed via collisions and coagulation. Spectral energy distributions (SED) indicate that grain growth, and the corresponding settling of large grains to the disk midplane, is occurring in some disks. Dust settling and growth affect disk temperatures and vertical structures, resulting in dust photospheres that are flatter rather than flared (e.g., D’Alessio et al. 1999; Chiang et al. 2001; Dullemond & Dominik 2004). Additionally, some main sequence stars show evidence of a “second generation” of small grains in a debris disk, produced by the collision and fragmentation of planetesimals, that may be

quite different from the “primordial” dust.

The spectroscopic study of silicate emission has proven a valuable tracer of grain processing within young circumstellar disks. This method probes small grains via optically thin emission from the surface layer of generally optically thick disks. Studies of $\sim 10\ \mu\text{m}$ silicate emission from Herbig Ae/Be stars (hereafter HAEBE) and T Tauri stars (hereafter TTs) with disks show early evidence of the growth of these surface-layer grains from ~ 0.1 to $2.0\ \mu\text{m}$ (see e.g., Bouwman et al. 2001; van Boekel et al. 2003). Detections of additional spectral features arising from crystalline silicate emission in some HAEBE and TTs disks (Waelkens et al. 1996; Sitko et al. 1999; Meeus et al. 2001; Honda et al. 2003; Acke & van den Ancker 2004), the debris disk β Pictoris (e.g., Knacke et al. 1993), and comets (see review by Wooden 2002) provide evidence for silicate processing during the disk phase. Although changes in grain size and composition are closely linked to disk properties and planet formation, the rate and mechanism of grain growth and processing in disks are still not well understood.

Previous studies of silicate emission from TTs disks were primarily focused on the Si-O stretching mode feature near $10\ \mu\text{m}$, which can be observed from the ground. Grain growth and crystallization, however, have similar effects on the shape of the $10\ \mu\text{m}$ feature. In these previous studies, the presence of crystalline silicates was often established through the presence of flux at $11.3\ \mu\text{m}$, corresponding to an emission feature of the crystalline Mg-rich silicate forsterite, in addition to the presence of an amorphous olivine feature at $9.8\ \mu\text{m}$. The combined effect is a broad, trapezoidal silicate emission feature with a peak near $9.7\ \mu\text{m}$ and a secondary peak near $11.3\ \mu\text{m}$. If crystalline silicates are abun-

¹ Department of Astronomy, University of Texas at Austin, 1 University Station C1400, Austin, TX 78712-0259, USA (jes@astro.as.utexas.edu)

² Leiden Observatory, PO Box 9513, 2300 RA Leiden, the Netherlands

³ Laboratoire d’Astrophysique de l’Observatoire de Grenoble, B.P. 53, 38041 Grenoble Cedex 9, France

⁴ Max-Planck-Institut für Astrophysik, P.O. Box 1317, D-85741 Garching, Germany

⁵ SRON, PO Box 800, 9700 AV Groningen, the Netherlands

⁶ Division of GPS, Mail Code 150-21, California Institute of Technology, Pasadena, CA 91125, USA

⁷ Division of PMA, Mail Code 105-24, California Institute of Technology, Pasadena, CA 91125, USA

⁸ Harvard-Smithsonian Center for Astrophysics, 60 Garden Street, MS42, Cambridge, MA 02138

dant, the feature can appear broader and flatter. In contrast, growth of amorphous olivines can mimic the effects of crystalline-amorphous silicate mixtures, resulting in weaker, “flat-topped” 10 μm silicate features, with similar flux at 9.8 and 11.3 μm (e.g., van Boekel et al. 2003; Przygodda et al. 2003; Kessler-Silacci et al. 2005). Indeed, the above studies showed that the flattened silicate features were well matched by models of purely amorphous olivines with grain sizes (radii) of 2 μm . Therefore, evaluation of the grain size and/or crystallinity requires observations of a larger spectral region, in which the presence of distinct forsterite or enstatite features (and PAHs, which emit near 7.7, 8.5, and 11.2 μm) can be assessed. Complementary studies of the O-Si-O bending mode near 20 μm probe slightly cooler dust and combined give a better sense of the grain size and crystalline fraction in the disk.

Spectra covering a large spectral region, including several isolated crystalline silicate features (27.5, 33.5, 35.8 and 70 μm), were obtained for disks around HAEBE stars (and some TTs) with the Infrared Space Observatory (ISO). ISO observations of several disks around intermediate-mass HAEBE stars clearly established the presence/absence of crystalline silicates (see Molster & Waters 2003; van Dishoeck 2004, for reviews). Additionally, ISO observations probed the ~ 10 and ~ 20 μm emission features from amorphous silicates in HAEBE disks, allowing grain growth to be studied (see Acke & van den Ancker 2004, for a review). Due to sensitivity limitations, ISO studies of silicates focused primarily on intermediate or high-mass stars. Studies of TTs have therefore been limited, for the most part, to the 10 μm region. Although changes in the shape of the 10 μm emission features are observed in small samples of TTs (Przygodda et al. 2003; Kessler-Silacci et al. 2005), the cause of these changes is unclear and could be a combination of silicate grain growth and crystallization.

In this study, the improved sensitivity of the Infrared Spectrograph (IRS) aboard the Spitzer Space Telescope was used to expand such spectroscopic studies to include a large sample of disks around low-mass, sun-like stars, creating a database analogous to ISO studies of \sim high/intermediate-mass stars. A few HAEBE stars were also observed for comparison. The data presented here are part of the c2d Spitzer legacy program designed to study the evolution of circumstellar matter ‘From Molecular Cores to Planet-Forming Disks’ (Evans et al. 2003). This paper contains preliminary results from the program and will focus on statistical analysis of the strongest silicate features. It will be followed by a more detailed study of weaker features, including emission from crystalline silicates. The Spitzer IRS observations are described in §2. In §3, an inventory of the most prominent silicate emission features will be presented. The observed spectra will be compared with models of amorphous silicates in §4. We perform a statistical analysis of the 10 and 20 μm silicate features and interpret these trends in terms of grain growth in §5. Then in §6, we examine the relationship between the strength-shape trends found in §5 and spectral type, stellar age, and $H\alpha$ equivalent width. Finally, in §7, we discuss the crystalline silicate emission features in the observed spectra.

2. OBSERVATIONS

Spectra for 40 solar-mass T Tauri stars and 7 intermediate-mass HAEBE stars were obtained using the Infrared Spectrograph (IRS) aboard the Spitzer Space Telescope from December 2003 through December 2004. The observations and

source parameters are described in Table 1 for the T Tauri stars (top) and HAEBE stars (bottom) in our sample. The spectra were observed with combinations of the short-low (SL), short-high (SH), long-low (LL), and/or long-high (LH) modules (see Table 1 column 4). SL ($\lambda = 5.3\text{--}14.5$ μm) and LL ($\lambda = 14.2\text{--}40.0$ μm) spectra have a resolving power of $R = \lambda/\Delta\lambda \sim 100$ and the SH ($\lambda = 10.0\text{--}19.5$ μm) and LH ($\lambda = 19.3\text{--}37.0$ μm) spectra have a resolving power of ~ 600 . For approximately half of the sources, SL spectra are part of the GTO programs and not yet available for analysis and, therefore, there is no spectral information short-ward of 10.0 μm . Exposure times were chosen to achieve signal-to-noise ratios of 50 and 100 for sources brighter and fainter than 500 mJy, respectively, with the weakest sources in our sample having fluxes of $\sim 100\text{--}200$ mJy at 15 μm . All sources in the c2d program (Evans et al. 2003) that were observed prior to December 2004 and show evidence of silicate emission are included (47 sources; see Table 1).

Data reduction was done via the c2d Interactive Analysis (c2dia) reduction environment. C2dia contains optimized extraction algorithms developed by the c2d legacy team⁹.

For wavelength calibration and IRS aperture definition, tools from the SMART¹⁰ software package (Higdon et al. 2004) were used. The extracted spectra were deFRINGED using the IRSFRINGE¹¹ package developed by the c2d team (Lahuis & Boogert 2003). The spectra were extracted from the Spitzer Science Center (SSC) Basic Calibrated Data (BCD), pipeline version S11.0.2¹². Two different extraction methods were used and compared to reduce spectral artifacts resulting from the extraction process.

The first method uses a full aperture extraction for SH and LH and fixed width aperture extraction for SL and LL. The extraction aperture was chosen to be large enough to enclose the complete source. (At the short wavelength end, the extraction aperture is wider than that used in the SSC pipeline. However, since the SL and LL spectra are corrected for the background, as described below, this has a negligible effect on the extracted spectrum.) Bad pixels are corrected by interpolating in the cross-dispersion direction using a fit to the order-averaged source profile. For SL and LL the the large apertures allow off-source spectra to be extracted and these spectra were used to make wavelength dependent background corrections. No background data were available for SH and LH spectra. A spectrum was extracted for each position, compared to check for artifacts, and finally averaged to produce the final spectrum.

In the second method, all BCDs from both dither positions are combined within the extraction algorithm. The extraction is performed by integrating over a source profile fit in the cross-dispersion direction. The source profile is a template created from standard star observations (including sky measurements for SH and LH). The width and center of this template is adjusted for each observed source in our sample to encompass 95% of the observed flux. This fitting process is

⁹ The c2d extraction algorithms will become publicly available through the Spitzer Space Science Center as part of the c2d legacy program.

¹⁰ The SMART software package is publicly available on the website <http://protecthttp://ssc.spitzer.caltech.edu/archanaly/contributed/smart>.

¹¹ IRSFRINGE is included in SMART and available as a stand-alone package from <http://protecthttp://ssc.spitzer.caltech.edu/archanaly/contributed/irsfringe/>.

¹² Recently data from the SSC pipeline version S12 as well as more advanced versions of the extraction algorithms have become available. We have verified that these do not have a significant impact on the reduced spectra and do not affect the results presented in this paper.

TABLE 1
SOURCE LIST

Source	RA (J2000)	DEC (J2000)	Observed Modules	AOR Key	Observation Date	Age (Myr)	H α EW ^a (Å)	Spectral Type	Ref.
RNO 15	03 27 47.68	+30 12 04.3	SL SH LH	0005633280	2004-08-30	...	116	...	1
LkH α 327	03 33 30.41	+31 10 50.4	SL SH LH	0005634560	2004-02-03	1.4	51–65	K2	1,2,3
LkH α 330	03 45 48.29	+32 24 11.8	SL SH LH LL1	0005634816	2004-10-25	...	11–20	G3	2,3
IRAS 03446+3254 S	03 47 47.12	+33 04 03.4	SL SH LH LL1	0005635072	2004-09-29
V710 Tau ^b	04 31 57.79	+18 21 36.3	SH LH	0005636608	2004-09-29	0.7/0.4	11/89	M0.5/M3	4
CoKu Tau 4	04 41 16.79	+28 40 00.5	SH LH	0005637888	2004-09-02	1.2–1.6	1.8–2.8	M1.5	2,5,6
IRAS 08267-3336	08 28 40.70	-33 46 22.3	SL SH LH LL1	0005639168	2004-11-11	...	25–35	K2–K3	7,8
SX Cha	10 55 59.74	-77 24 39.9	SH LH	0005639424	2004-08-31	1–4	26.7	M0.5	9–11
SY Cha	10 56 30.47	-77 11 39.4	SH LH	0005639424	2004-08-31	2–5	24–64	M0	9–12
TW Cha	10 59 01.11	-77 22 40.8	SH LH	0005639680	2004-09-01	20	26.1	M0	9,11
VW Cha ^b	11 08 00.53	-77 42 28.7	SH LH	0005639680	2004-09-01	0.4–0.9	72–147	K2	9–12
VZ Cha	11 09 23.80	-76 23 20.7	SH LH	0005640448	2004-09-02	4–10	58–71	K6	9–12
WX Cha ^b	11 09 58.75	-77 37 08.9	SH LH	0005640192	2004-09-01	1–5	65.5	K7–M0	9–11
ISO Cha237	11 10 11.44	-76 35 29.2	SH LH	0005640448	2004-09-02	...	<3	M0	13
C7-11 ^b	11 10 38.01	-77 32 39.9	SH LH	0005640192	2004-09-01	0.2–1	4.0	K3	9,14
HM 27	11 10 49.62	-77 17 51.7	SH LH	0005640192	2004-09-01	30–40	200.0	K7	9,11
XX Cha	11 11 39.67	-76 20 15.1	SH LH	0005640448	2004-09-02	2–40	133.5	M2	9–11
T Cha	11 57 13.53	-79 21 31.5	SH LH	0005641216	2004-07-18	>12.5	2–10.0	G2–G8	15–17
IRAS 12535-7623	12 57 11.78	-76 40 11.5	SH LH	0011827456	2004-08-31	...	3.0	M0	17,18
Sz 50	13 00 55.37	-77 10 22.2	SH LH	0011827456	2004-03-25	...	46	M3	19
HT Lup ^b	15 45 12.87	-34 17 30.6	SL SH LH	0009829120	2004-08-28	0.4–0.8	3–7	K2	11,12,20
GW Lup	15 46 44.68	-34 30 35.4	SL SH LH LL1	0005643520	2004-08-30	1.3–3.2	90–98	M2–M4	11,20,21
HM Lup	15 47 50.63	-35 28 35.4	SL LL1 LL2	0005643776	2004-08-30	1.2–2.7	115–155	M3	11,20
Sz 73	15 47 56.98	-35 14 35.1	SL SH LH LL1	0005644032	2004-08-30	2.6–5.4	97–150	K2–M0	11,20,21
GQ Lup	15 49 12.10	-35 39 05.0	SL SH LH LL1	0005644032	2004-08-30	0.1–0.6	31–39	K7–M0	11,12,20
IM Lup	15 56 09.17	-37 56 06.4	SL SH LH LL1	0005644800	2004-08-30	0.1–0.6	4.7–8.1	M0	11,12,20
RU Lup	15 56 42.31	-37 49 15.5	SL SH LH LL1	0005644800	2004-08-30	0.1–0.5	136–216	K7–M0	11,12,20
RY Lup	15 59 28.39	-40 21 51.2	SL SH LH LL1	0005644544	2004-08-30	1.6–3.2	7.3	K0–K4	12,20
EX Lup	16 03 05.52	-40 18 24.9	SL SH LH LL1	0005645056	2004-08-30	1.4–3.0	31–43	M0	11,12,20
Sz 102	16 08 29.70	-39 03 11.3	SL SH LH	0009407488	2004-03-25	...	377	K0–M4	20
AS 205 ^b	16 11 31.35	-18 38 26.1	SL SH LH	0005646080	2004-08-28	0.1	55–155	K5/M3	2,3,12,22
VSSG1	16 26 18.86	-24 28 19.7	SH LH	0005647616	2004-08-28
DoAr 24E ^b	16 26 23.38	-24 21 00.1	SH LH	0005647616	2003-12-15	1.5	5	K0	22,23
GY23	16 26 24.06	-24 24 48.1	SH LH	0005647616	2004-08-28	K5–M2	24
SR 21 N	16 27 10.28	-24 19 12.5	SH LH	0005647616	2003-12-15	1	0.54	G1–G2.5	22,25
SR 9 ^b	16 27 40.27	-24 22 04.0	SH LH	0012027392	2004-09-02	...	6–14	K5–M2	2,23,24,26
Haro 1-17	16 32 21.94	-24 42 14.7	SL SH LH LL1	0011827712	2004-08-29	...	15	M2.5	26
RNO 90	16 34 09.18	-15 48 16.8	SL SH LH LL1	0005650432	2004-08-28	6	76	G5	1
EC 82	18 29 56.89	+01 14 46.5	SL SH LH	0009407232	2004-03-27	...	5–11	M0	2,27
CK 4	18 29 58.21	+01 15 21.7	SL SH LH	0009407232	2004-03-27
BF Ori	05 37 13.26	-06 35 00.6	SL SH LH LL1	0005638144	2004-10-03	2.0	6–11	A5–F6	2,12,28–30
RR Tau	05 39 30.52	+26 22 27.0	SL SH LH LL1	0005638400	2004-09-28	0.6	21.2–50	B8–A5	2,28,29,31
HD 98922	11 22 31.67	-53 22 11.4	SH LH	0005640704	2004-01-04	...	27.9	B9	30,31
DL Cha	13 06 08.36	-77 06 27.3	SH LH	0005642240	2004-07-14	M6	22
HD 135344	15 15 48.44	-37 09 16.0	SH LH	0005657088	2004-08-08	17	17.4	A0–F4	30,32–34
HD 163296	17 56 21.29	-21 57 21.9	SH LH	0005650944	2004-08-28	4–6	12–17	A0–A2	15,29–32
VV Ser	18 28 47.86	+00 08 39.8	SL SH LH	0005651200	2004-09-01	0.6	22–90	B1–A3	3,28–31

REFERENCES. — (1) Levreault 1988; (2) Cohen & Kuhl 1979; (3) Fernandez et al. 1995; (4) Hartigan et al. 1994; (5) D’Alessio et al. 2005; (6) Kenyon et al. 1998; (7) Reipurth & Pettersson 1993; (8) Sahu & Sahu 1992; (9) Lawson et al. 1996; (10) Hartmann et al. 1998; (11) Appenzeller et al. 1983; (12) Reipurth et al. 1996; (13) Saffie et al. 2003; (14) Hartigan 1993; (15) van den Ancker et al. 1998; (16) Alcalá et al. 1995; (17) Gregorio-Hetem et al. 1992; (18) Sartori et al. 2003; (19) Hughes & Hartigan 1992; (20) Hughes et al. 1994; (21) Heyer & Graham 1989; (22) Prato et al. 2003; (23) Bouvier & Appenzeller 1992; (24) Luhman & Rieke 1999; (25) Martin et al. 1998; (26) Rydgren 1980; (27) Gomez de Castro 1997; (28) Natta et al. 1997; (29) Finkenzeller & Mundt 1984; (30) Acke et al. 2005; (31) The et al. 1994; (32) Thi et al. 2001; (33) Houk 1982; (34) Dunkin et al. 1997.

NOTE. — Sources in the top portion of the table are T Tauri stars; sources in the bottom portion are HAEBE stars.

^aAll H α lines are in emission, except that of SR 21, which is in absorption

^bThis source is a binary in 2MASS K-band images, with a separation < 3'', and is unresolved with Spitzer IRS. Spitzer IRS observations are pointed at the center of the binary system. Stellar/disk parameters quoted from the literature include both sources.

performed for each source by using the highest quality data. Once the source profile is fit, a (uniform) local sky background level, which is wavelength dependent, is estimated. This method also reduces the effects of unidentified bad pixels. In particular, in cases where the BCD images are largely affected by bad pixels (e.g., for LH), this method quite often gave significant improvements over the full aperture extrac-

tion. In the version of c2dia used here, the wavelength and flux calibration files produced by SSC pipeline were used. For the S12 version of c2dia, the extraction algorithm is further developed and independently calibrated using a suite of standard star calibrators. The extraction algorithms and the calibration involved will be described in more detail in Lahuis (in

prep.).

To correct for the possibly significant sky contribution in the SH and LH spectra, spectra obtained using full aperture extraction were corrected using the background estimate from the source profile fitting extraction method. Both extractions were also compared against the spectra extracted from the SSC pipeline. In a few cases, particular modules suffered from artifacts due to data selection and/or bad-pixel correction and the corresponding modules of the SSC spectrum were used. In cases where the SSC spectra were used, a correction to the zero level was applied to correct for background emission. Good sections of the background corrected spectra were used to estimate the zero level in the other modules. When necessary, individual orders and/or modules were multiplied by small ($< 5\%$ and $< 15\%$, respectively) constant factors to correct flux offsets between orders/modules. These flux offsets are likely related to pointing errors resulting in the source not being centered in the aperture and seem to be corrected in the SSC pipeline version S12.

3. INVENTORY OF SILICATE EMISSION FEATURES

The extracted spectra of TTs and HAEBE disks are shown in Figure 1 and Figure 2, respectively. Two sources, HT Lup and HD 163296, were observed twice, once in IRS-staring mode and once in spectral mapping mode. The two observations for each source do not differ significantly; integrated intensities, peak-to-continuum fluxes, and feature widths agree to within $\sim 7\%$ for the 10 and 20 μm features. Therefore, only one spectrum for each source is included in Figures 1 and 2 and Table 2.

An inventory of the silicate emission features is presented in Table 2. The features listed are relatively isolated and can be clearly identified in the spectra. The peak wavelengths of the silicate features depend on the exact composition and grain size of the dust. Therefore, the broad amorphous silicate features, corresponding to the Si-O stretching and O-Si-O bending modes, are labeled as ~ 10 and ~ 20 μm . The peaks of the identified crystalline silicate features may vary within the wavelength ranges given in Table 2, which correspond to the ranges in peak wavelengths for features of crystalline enstatite and forsterite of sizes between 1 and 10 μm . Features are marked with “Y”, “T”, or “N” if the feature is detected, tentatively detected, or absent.

Emission at 10 and 20 μm from amorphous silicates dominates the spectra of most of the disks observed. Broad 20 μm amorphous silicate features can be seen in almost all of the spectra, while the 10 μm amorphous silicate features are slightly less prominent (seen in 42 of 47 spectra). Emission near 11.3 μm , due to PAH or crystalline forsterite, is clearly identified in $\sim 1/3$ of the spectra. This is a lower limit, however, as tentative emission is seen in several additional spectra in which the presence of artifacts prevent further analysis. ISO observations of disks around HAEBE stars (Acke & van den Ancker 2004) report 11.3 μm emission from $\sim 1/4$ of the observed sources, but the same studies find that the fraction showing PAH emission at 7.7 μm is much higher (57%).

The lattice modes of crystalline silicates at $\lambda > 25$ μm appear to be more prominent than the 11.3 μm feature in our data and do not suffer from confusion with PAH emission. Approximately half of the disks in our sample show emission features near 28 μm and in the 33-35 μm region, characteristic of crystalline enstatite and forsterite. The 24 to 36 μm region is shown for 6 of these sources in Figure 3, with shaded re-

gions depicting the typical positions of enstatite and forsterite features. These data indicate that crystalline silicates can be quite prominent in TTs disks. This is in surprising contrast to ground-based studies of silicates in the 10 μm region, which found crystalline silicate emission from very few TTs (see Kessler-Silacci et al. 2005, for summary).

As the 10 and 20 μm emission features from amorphous silicates are the most easily identified and isolated, the rest of this paper will focus on the analysis of these features. PAHs will be discussed in detail in Geers et al. (in prep.) and SEDs will be modeled in Augereau et al. (in prep.). Silicate composition will be modeled in more detail by Kessler-Silacci et al. (in prep.), including analysis of all crystalline silicate features.

4. COMPARISONS WITH MODELS OF AMORPHOUS SILICATES

As mentioned above, the peak wavelengths, strengths and shapes of the silicate features depend on the exact composition, sizes, and shapes of the silicates. Therefore, in order to interpret the observed silicate emission, we must compare our data with models of the emission from a variety of silicate grains. Modeled grain opacities can be compared to the observed emission once the continuum is removed. In §4.1, we describe the method of continuum normalization used here. Our procedure for modeling of grain opacities from laboratory optical constants is described in §4.2. Finally, in §4.3, we will quantitatively compare modeled and observed opacities in the 10 and 20 μm regions.

4.1. Continuum normalization

Continuum normalization was performed using one of three methods, as noted in Table 2, and described as:

1. For spectra that include SL (e.g., RNO 15), a 2nd order polynomial was fit to the continuum in the following regions: 6.8–7.5 μm , 12.5–13.5 μm , and 30–36 μm .
2. For spectra that do not include SL (e.g., V710 Tau), the continuum was obtained with a linear fit to the 12.5–13.5 μm and 30–36 μm regions.
3. In cases where the SED appears to fall sharply with increasing wavelength short-ward of 12–15 μm and then rises sharply beyond ~ 15 μm (e.g., LkH α 330), we fit the 10 and 20 μm features separately, using a 2nd order polynomial fit for wavelengths short-ward of ~ 15 μm and a linear fit long-ward of ~ 15 μm . These sources will be discussed in more detail in Brown et al. (in prep.).

The continuum fits are overlaid on the observed spectra in Figures 1 and 2 as dash-dotted lines. The continuum fitting regions were chosen to represent the areas least affected by features in the spectra and, as shown, vary slightly from source to source. Opacities obtained from laboratory spectra of amorphous olivines (see §4) indicate that the regions chosen above should be clear of amorphous silicate emission features, with the exception of the region from ~ 13 –15 μm , which likely contains contributions from the wings of both the 10 and 20 μm features. Thus, the feature strengths obtained from the continuum normalized spectra will be underestimated.

After the continuum fitting was performed, the normalized spectra S_ν were obtained via application of the formula,

$$S_\nu = 1 + \frac{(F_\nu - F_{\nu,c})}{\langle F_{\nu,c} \rangle},$$

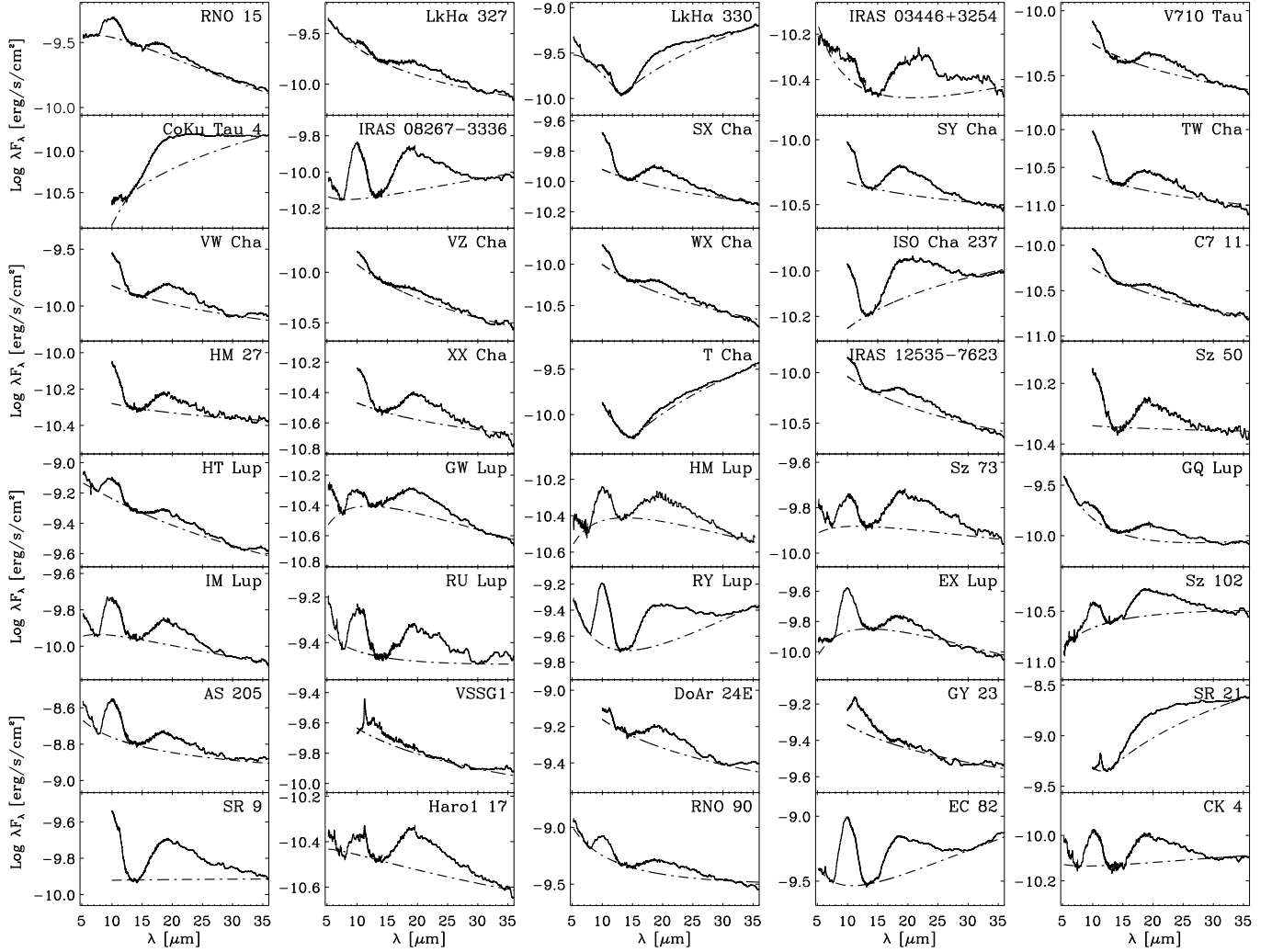


FIG. 1.— Spitzer mid- to far-IR spectra for T-Tauri disks. The spectra for each source are shown in units of $\text{Log } \lambda F_{\lambda}$. The SH and LH spectra have been median smoothed over 3 and 5 channels, respectively. No smoothing has been applied to the other modules. The dash-dot line denotes the fit to the continuum described in the text and Table 2.

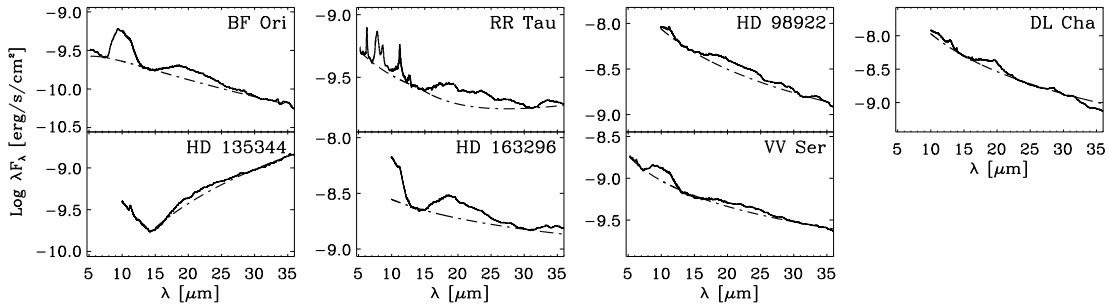


FIG. 2.— Spitzer mid- to far-IR spectra for HAEBE disks. The spectra for each source are shown in units of $\text{Log } \lambda F_{\lambda}$. The SH and LH spectra have been median smoothed over 3 and 5 channels, respectively. No smoothing has been applied to the other modules. The dash-dot line denotes the fit to the continuum described in the text and Table 2.

where F_{ν} is the observed spectrum and $F_{\nu,c}$ is the fitted continuum, both in units of Jy, and $\langle F_{\nu,c} \rangle$ is the frequency averaged continuum flux. We divide by a frequency averaged value of the continuum flux in order to remove any dependence on the slope of the continuum. This normalization method, including the offset of 1.0, is consistent with the method used by van Boekel et al. (2003) and Przygodda et al.

(2003), to which we compare in §5. As the continuum may change dramatically between 10 and 20 μm for some sources (e.g., CoKu Tau 4), $\langle F_{\nu,c} \rangle$ is calculated separately for regions of $\lambda = 5\text{--}13 \mu\text{m}$ and $\lambda = 13\text{--}37 \mu\text{m}$. If $F_{\nu,c}$ is used in place of $\langle F_{\nu,c} \rangle$, then the normalization would reduce to $F_{\nu}/F_{\nu,c}$, which is approximately equal to the optical depth

TABLE 2
SILICATE EMISSION FEATURES

Species $\lambda(\mu\text{m})$	Silicates ^a ~10	PAH/Cr.Sil. ^b 11.2-11.3	Silicates ^a ~20	Cr.Sil. ^c 28-29	Cr.Sil. ^d 33-35	Norm. ^e Method
RNO 15	Y	T	T	Y	T	1
LkH α 327	Y	Y	Y	Y	Y	1
LkH α 330	Y	Y	Y	T	N	3
IRAS 03446+3254	Y	Y	Y	N	T	1
V710 Tau	Y	T	Y	T	T	2
CoKu Tau 4	Y	T	Y	N	N	2
IRAS 08267-3336	Y	N	Y	N	N	1
SX Cha	Y	T	Y	T	Y	2
SY Cha	Y	T	Y	T	T	2
TW Cha	Y	T	Y	T	T	2
VW Cha	Y	T	Y	Y	Y	2
VZ Cha	Y	T	T	Y	Y	2
WX Cha	Y	T	Y	T	Y	2
ISO Cha237	Y	T	Y	T	T	2
C7-11	Y	T	Y	T	T	1
HM 27	Y	N	Y	T	T	2
XX Cha	Y	N	Y	T	T	2
T Cha	N	Y	T	N	N	3
IRAS 12535-7623	Y	T	Y	Y	N	2
Sz 50	Y	N	Y	N	T	2
HT Lup	Y	T	Y	T	Y	1
GW Lup	Y	T	Y	T	T	1
HM Lup	Y	T	T	T	T	1
Sz 73	Y	T	Y	T	T	1
GQ Lup	Y	T	Y	Y	Y	1
IM Lup	Y	T	Y	T	T	1
RU Lup	Y	T	Y	Y	Y	2
RY Lup	Y	N	Y	N	N	1
EX Lup	Y	T	Y	T	T	1
Sz 102	Y	T	Y	N	Y	1
AS 205	Y	T	Y	T	T	1
VSSG1	Y	Y	N	Y	T	2
DoAr 24E	Y	Y	Y	Y	T	2
GY23	N	Y	N	Y	T	2
SR 21	N	Y	Y	T	T	3
SR 9	Y	T	Y	T	N	2
Haro 1-17	Y	Y	Y	Y	Y	1
RNO 90	Y	N	Y	T	N	1
EC 82	Y	N	Y	N	T	1
CK 4	Y	T	Y	T	Y	1
BF Ori	Y	T	Y	T	Y	1
RR Tau	N	Y	Y	Y	Y	1
HD 98922	T	Y	Y	Y	Y	2
DL Cha	T	Y	Y	Y	N	2
HD 135344	N	Y	T	N	N	3
HD 163296	Y	T	Y	T	Y	2
VV Ser	Y	T	Y	T	Y	1

NOTE. — Features are marked with a “Y” if detected, “N” if not detected, or “T” if the identification is tentative.

^aBroad, primarily amorphous olivine/pyroxene emission features.

^bFeature includes PAH at 11.2 μm and crystalline forsterite at 11.3 μm (Geers et al., in prep.).

^cFeature includes crystalline forsterite near 27.9 μm and/or crystalline enstatite near 28.5 μm

^dFeature includes crystalline forsterite near 33.6 μm and/or crystalline enstatite near 34.5 μm

^eContinuum normalization procedure as described in the text

for optically thin emission;

$$\frac{F_\nu}{F_{\nu,c}} = 1 - e^{-\tau_\nu} \approx \tau_\nu \quad (\tau_\nu \ll 1),$$

where τ_ν is the optical depth as a function of frequency. Comparison between the two continuum normalization methods for the spectra in the c2d sample shows that the 10 and 20 μm feature strengths and shapes do not differ significantly ($\sim 5\%$ and $\sim 10\%$, respectively).

Although continuum normalization has been previously used to interpret ground-based and ISO observations of 10 μm silicate emission features (Honda et al. 2003; van Boekel et al. 2003; Przygodda et al. 2003; Acke & van den Ancker 2004), it was previously not applied to 20 μm silicate features because the emission feature strength can be confused by a rising continuum. To address this issue, we plot the spectral index (α) of the derived continuum from 13 to 35 μm versus the strength of the continuum normalized 20 μm feature ($S_{peak}^{20\mu\text{m}}$) in Figure 4.

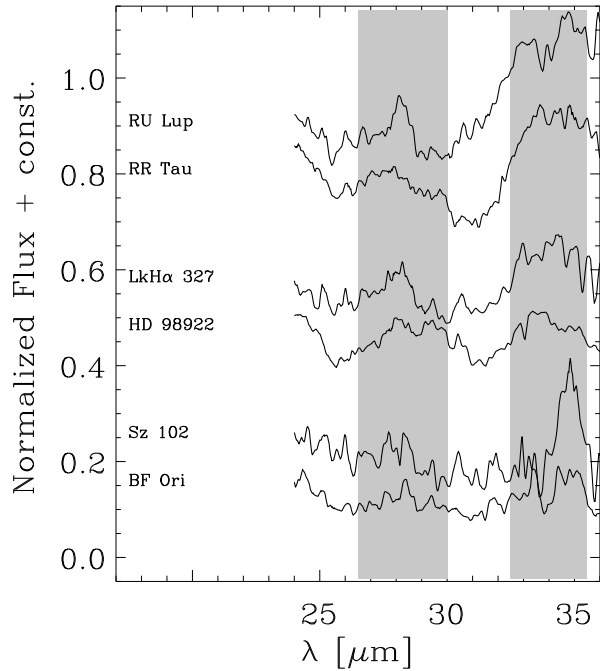


FIG. 3.— Continuum normalized and smoothed LH spectra for 6 of the sources that show emission from crystalline silicates in the 26.5–30 and/or 33–35 μm regions (depicted by shading). Each pair of spectra contains one HAEBE star (bottom) and one T Tauri star (top). Features in the 26.5–30 μm region tend to be narrower for the T Tauri stars.

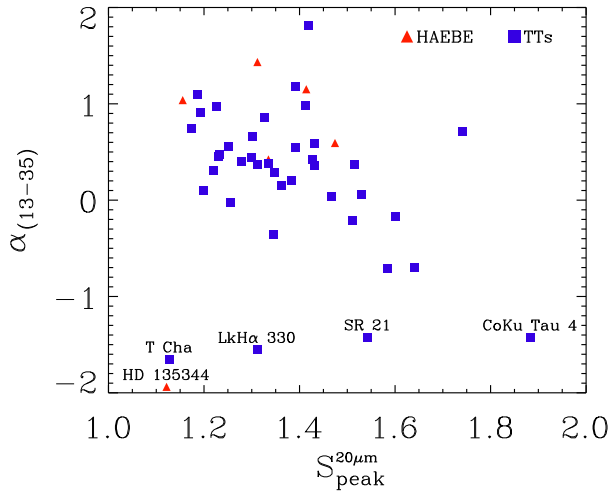


FIG. 4.— Evaluation of the continuum normalization method at 20 μm . 13–35 μm spectral indices are plotted versus the strengths of the continuum normalized 20 μm silicate emission features for all sources. TTs are denoted by filled squares and HAEBE are denoted by filled triangles. The mid-IR spectral indices and 20 μm feature strengths appear to be at most weakly inversely correlated ($r = -0.2$, 80% significance), with more steeply rising spectra corresponding to stronger 20 μm silicate emission features.

The spectral indices are calculated as,

$$\alpha_{a-b} = -\frac{\text{Log}(\lambda_b F_{\lambda_b}) - \text{Log}(\lambda_a F_{\lambda_a})}{\text{Log}(\lambda_b) - \text{Log}(\lambda_a)}$$

where $\lambda_a = 13 \mu\text{m}$, $\lambda_b = 35 \mu\text{m}$, and F_{λ_x} is the flux-density at wavelength λ_x in units of $\text{erg cm}^{-2} \text{s}^{-1} \mu\text{m}^{-1}$. The bulk of the spectra are relatively flat or falling in units of λF_{λ} , with $\alpha = 0$ –1 and $S_{peak}^{20\mu\text{m}} = 1.1$ –1.5 (see Figure 4). The five sources for which we use continuum fitting method 3 have

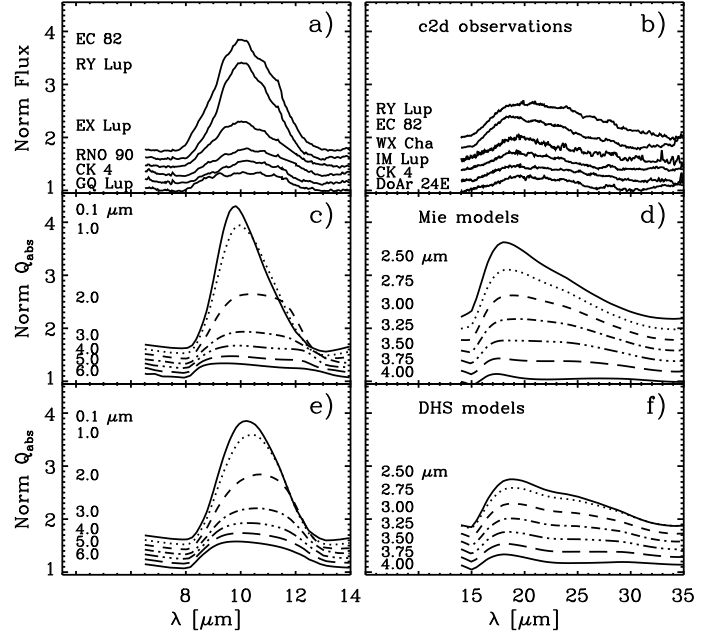


FIG. 5.— Evidence of grain growth in the Si-O stretching and O-Si-O bending mode features. The top panels show the observed normalized spectra in the a) 10 μm and b) 20 μm regions for sub-samples of our sources. The bottom two panels show the normalized absorption efficiencies (Q_{abs}) for models of spherical grains of amorphous olivines with various grain sizes calculated for the 10 μm and 20 μm regions. Models of filled homogeneous spheres calculated using Mie theory are shown in c) and d) and models of hollow spheres calculated using DHS theory are shown in e) and f). Spectra in all panels have been artificially shifted along the y-axis by a constant value as a function of wavelength, such that the spectrum of each source could be seen more clearly. The minimum of each normalized spectra was 1.0 prior to adding these constants.

spectra that are steeply rising from 13 to 35 μm ($\alpha = -1$ to -2) and lie along the bottom of Figure 4. A few other sources with rising spectra (e.g., RY Lup, EC 82) can be seen in the right of Figure 4. We find that the spectral index and the derived strength of the 20 μm feature is at most weakly correlated (at the 80% significance level), with the more steeply rising spectra corresponding to the stronger 20 μm silicate features. There is thus a small chance that the shape/strength parameters derived for a particular source may be related to the continuum fit. As stated above, modeling of individual spectra without continuum normalization will be presented in Kessler-Silacci et al. (in prep.).

A representative sample of continuum normalized spectra in the 10 and 20 μm regions are shown in Figure 5a,b. A large fraction of the observed spectra are similar to GQ Lup, possessing weak, and sometimes flat-topped 10 μm silicate emission features. A few others possess centrally peaked 10 μm features, with large peak-to-continuum flux, as is the case for EC 82. The rest of the sample falls between these two extremes. Most spectra show 20 μm features with lower peak-to-continuum flux in the 20 μm region with respect to that at 10 μm .

4.2. Modeling dust optical properties

To aid in the interpretation of the observed silicate emission features, we model the opacities for a sample of grains of different shape, size and composition. Optical constants are obtained from laboratory data available from the Jena –

TABLE 3
LIST OF ADOPTED GRAIN MATERIAL

Dust type	Formula/Name	Refs
amorphous olivine	MgSiO ₄	Dorschner et al. (1995)
amorphous pyroxene	Mg _{0.5} Fe _{0.5} SiO ₃	Dorschner et al. (1995)
crystalline forsterite	Mg ₂ SiO ₄	Servoin & Piriou (1973)
crystalline enstatite	MgSiO ₃	Jäger et al. (1998)
amorphous carbon	ACAR	Zubko et al. (1996)

St. Petersburg database¹³ (Henning et al. 1999, see Table 3). Absorption efficiencies (Q_{abs}) are then calculated for spherical, homogeneous grains of different sizes, representing compact grains, using Mie theory (Mie 1908). Interstellar dust, however, is not likely to be spherical and images of interplanetary dust particles (see Bradley 2003, for review) suggest that nebular dust likely consists of porous and irregularly shaped aggregates. Additionally, the positions of the features in the mass absorption coefficients of crystalline silicates derived via Mie theory do not agree with observations of astronomical silicates (e.g., Bouwman et al. 2001). Therefore, to simulate porous or irregularly shaped particles, we calculate opacities for continuous distributions of hollow spheres (DHS), using the statistical method described in Min et al. (2005). In the Mie method, the particle can be represented by a homogeneous, filled sphere. In the DHS method, a distribution of hollow spherical silicate shells is used such that the vacuum volume filling fractions vary, but the masses remain the same as that of the homogeneous, filled sphere. The DHS method averages the scattering and absorption/emission cross sections of the set of hollow spheres and these cross sections can be compared to those of the homogeneous filled sphere of the same mass. The optical properties of individual large hollow spheres are calculated using the algorithm proposed by Toon & Ackerman (1981) for coated spheres, which was found to be extremely accurate (to 4 decimal places) when compared to measured efficiencies. We apply a simple analytical application of the Rayleigh approximation as described in Min et al. (2003) for small grains with $x = 2\pi a/\lambda \ll 1$ and $|mx| \ll 1$, where a is the radius of the particle and m is the refractive index.

Figures 6–8 show the absorption efficiencies (Q_{abs}) for grains of amorphous olivine, pyroxene, and crystalline forsterite for a range of sizes between 0.1 and 10 μm . Here we have used the grain radius (a) of the filled, homogeneous sphere as a proxy for the grain mass, which is held constant for both Mie and DHS models. As indicated in Figure 6, the slope of the overall spectrum varies significantly as a function of grain size. Thus, in order to compare the model Q_{abs} to the normalized Spitzer spectra, we use a “continuum” fitting method which is similar to that applied to the Spitzer spectra. Although this method will most likely not find the physical continuum level, treating the observed and modeled spectra in the same manner will enable a more robust comparison. Normalized Q_{abs} in the 10 and 20 μm regions for the modeled grain opacities of amorphous olivines calculated using Mie and DHS are shown in Figure 5c,d and Figure 5e,f, respectively. The comparison of these normalized absorption efficiencies to the observed spectra involves an implicit assumption about the dominance of silicate emission in the 8–35 μm

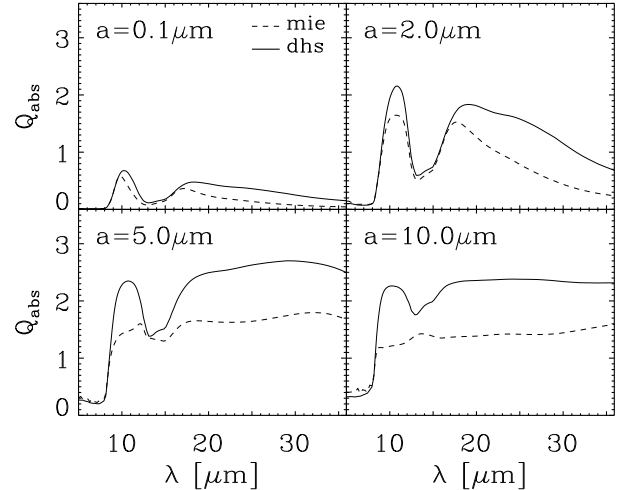


FIG. 6.— Absorption efficiencies for amorphous olivine for grain sizes of 0.1, 2, 5, and 10 μm . In the upper left panel, Q_{abs} for $a = 0.1 \mu\text{m}$ has been multiplied by a factor of 5. The dashed lines show Q_{abs} calculated using Mie theory for spherical grains. The solid lines show Q_{abs} calculated using the distribution of hollow spheres (DHS) method described in the text.

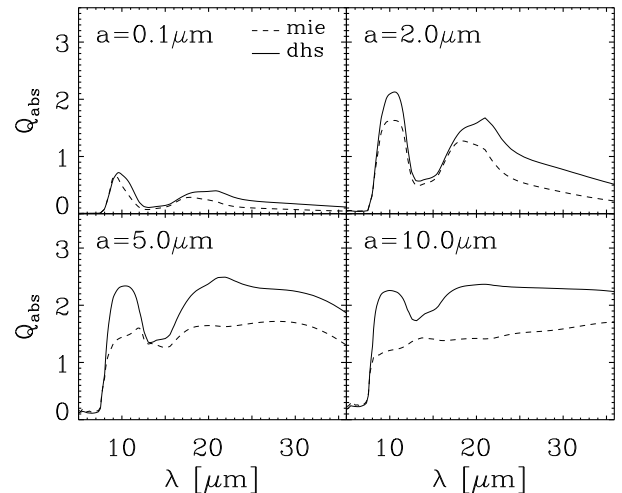


FIG. 7.— Absorption efficiencies for amorphous pyroxene for grain sizes of 0.1, 2, 5, and 10 μm . In the upper left panel, Q_{abs} for $a = 0.1 \mu\text{m}$ has been multiplied by a factor of 5. Lines are as in Figure 6.

region. Disk models (e.g., Pollack et al. 1994) based on solar elemental abundances find that the main refractory components are olivine, pyroxene, carbonaceous material and/or organics, water ice, troilite (FeS) and metallic iron. They find that silicates clearly dominate the opacity for $T > 500$ K, but at lower temperatures the shapes and strengths of the 10 and 20 μm features can be affected by the opacities of organics and water ice. The silicate emission studied here arises from the warm surface layers of these disks and ices are unlikely to play any role. Additionally, the excellent correspondence between the modeled silicate opacities and the observed spectra (cf. Figure 5), in both contrast and spectral shape, suggest that we are in a regime in which this comparison is valid.

4.3. Grain growth

¹³ <http://www.astro.uni-jena.de/Laboratory/Database/databases.html>

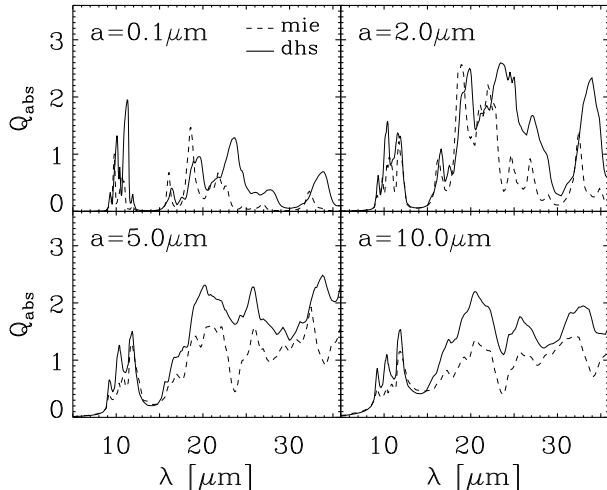


FIG. 8.— Absorption efficiencies for crystalline forsterite for grain sizes of 0.1, 2, 5, and 10 μm . In the upper left panel, Q_{abs} for $a = 0.1\mu\text{m}$ has been multiplied by a factor of 5. Lines are as in Figure 6. Note that the results of Mie/DHS theory for large ($a > 2\mu\text{m}$) forsterite grains have not been confirmed by laboratory studies. Additionally, emission feature positions are offset for Mie and DHS models. DHS models have been found to more closely agree with astronomical observations of silicates in disks (van Boekel et al. 2005).

Both the shape and strength of the silicate features are dependent upon grain size, with Mie and DHS models possessing slightly different silicate features. In this section we will compare the 10 and 20 μm silicate features in the observed spectra to the Mie and DHS models (Figure 5).

Both Mie and DHS models show that the 10 μm silicate feature strength decreases, and the feature flattens, as a function of grain size. The 10 μm feature strength for Mie models (Figure 5c) is largest for grain sizes of $a \approx 0.1\mu\text{m}$. When $a = 8\mu\text{m}$, the feature has almost disappeared. A similar trend can be seen in the models of hollow spheres using DHS methods in Figure 5e. The shape of the 10 μm feature is slightly more round for the DHS than Mie models, however, and the peak strength is underestimated (with respect to Mie models) for smaller grain sizes ($a = 0.1\mu\text{m}$) and overestimated for larger grain sizes ($a = 6.0\mu\text{m}$).

For the 20 μm feature (Figure 5d,f), again we see that for both Mie and DHS models, the feature strength decreases and broadens when the grain size is increased from 2.5 to 5.0 μm . The emission feature also appears to shift to longer wavelength with increasing grain size, peaking near 18 μm (similar to our observations) for Mie and DHS models of amorphous olivines with grain sizes of $a = 3\text{--}5\mu\text{m}$. The shapes of the 20 μm features of the Mie and DHS models are also slightly different, with DHS models showing a much flatter feature. Additionally, the peak strengths of the DHS models are smaller than those of the Mie models for smaller grain sizes ($a = 2.5\mu\text{m}$) and larger than the Mie models for larger grain sizes ($a = 4.0\mu\text{m}$).

The observed spectra (Figure 5a,b) are quite similar to the models, differing slightly for the weakest emission features. The weakest 10 μm features observed toward several sources are similar to the models of 5 μm amorphous olivine grains, but appear to be slightly narrower and more sharply peaked at the edges of the feature. Additional emission from crystalline silicates may be necessary to reproduce the “boxy” structure

of such features. The strongest observed 20 μm features are similar in strength to models of amorphous olivine with grain sizes $> 2\mu\text{m}$. The weakest features are similar in strength to models of amorphous olivine with sizes less than approximately 4.5 μm .

Thus, the comparison of the observed spectra with modeled amorphous olivine opacities provides a qualitative understanding of the effect of grain growth on the 10 and 20 μm features observed for our sample. In the following section, we will perform a more quantitative analysis.

5. STATISTICAL ANALYSIS OF THE 10 AND 20 μm FEATURES

Previous observations of disks around HAEBE and T Tauri stars have shown that plots of the shape vs. strength of the 10 μm emission feature may be indicative of grain growth. In §5.1 we interpret variations in the shape and strength of the observed silicate features in terms of source-to-source variations in grain size. Because it is important to understand the uniqueness of this interpretation, in §5.2 we evaluate the dependence of the 10 and 20 μm feature strengths on several other grain properties, including the grain size distribution, relative sizes of grains emitting at 10 and 20 μm , grain composition, crystallinity, and porosity.

5.1. Strength-shape trends

We find that the shapes of the continuum normalized 10 μm emission feature from HAEBE and TTs are proportional to the feature strengths (as was previously noted by van Boekel et al. 2003, and later Przygodda et al. 2003 and Kessler-Silacci et al. 2005). In Figure 9a, we plot the shape of the 10 μm feature versus the feature strength, $S_{peak}^{10\mu\text{m}}$. As a proxy for the feature shape, we use the ratio of the normalized flux at the peak of the crystalline silicate feature relative to that of the amorphous silicate feature ($S_{11.3}/S_{9.8}$). The fluxes are integrated over regions of $\pm 0.1\mu\text{m}$ around the central wavelength. Data from the literature (*lit*, van Boekel et al. 2003; Przygodda et al. 2003; Kessler-Silacci et al. 2005 open symbols) are plotted in addition to the data collected in this study (*c2d*, filled symbols). Source parameters and original references for the *lit* sample are listed in Table 4. There are five sources that overlap between the *c2d* and *lit* samples: RU Lup, AS 205, DoAr 24E, HD 98922, and HD 163296. The 10 μm feature strengths and shapes of these sources are consistent to within $11 \pm 7\%$. In the statistical analysis, we use only our data for the duplicate sources, except in the case of AS 205 for which we will use the Przygodda et al. (2003) spectra for each source in the binary. There is a strong correlation for the entire sample of 10 μm features, which is consistent with that first noted by van Boekel et al. (2003). This trend is similar to changes in silicate emission due to grain size variations illustrated in Figure 5, with flatter, weaker 10 μm emission features, characteristic of larger grain sizes, appearing in the upper left of Figure 9a.

In order to interpret this trend more quantitatively, we perform the same analysis for the continuum normalized model opacities discussed in §4.2. We include grains of amorphous olivine, pyroxene, and mixtures of the two for grain sizes between 0.1 and 20 μm . The Maxwell–Garnett mixing rule (Maxwell Garnett 1904) is used to calculate effective cross sections for all mixtures. The model data are overlaid on the observational data in Figure 9a, with lines connecting points of varying grain size for each model. Note that the peak strength corresponds to different sizes depending on the dust

TABLE 4
STELLAR/DISK PARAMETERS FOR MIR SPECTRA FROM THE LITERATURE

Source	RA ^a (J2000)	DEC ^a (J2000)	Spect. ^b Ref.	Age (Myr)	H α EW ^c (Å)	Spectral Type	Ref.
GG Tau ^d	04 32 30.31	+17 31 41.0	Prz	1.7	31–54	K6–K7	1,2,3
AA Tau	04 34 55.45	+24 28 53.7	K-S	0.9–2.4	37.1	K7	1,2,4,5
Lkca 15	04 39 17.80	+22 21 04.5	K-S	2–11	23.1	K5	1,4,6
DR Tau	04 47 05.48	+16 58 42.1	Prz	3.8	95.4	K4	1,2
GM Aur	04 55 10.90	+30 22 01.0	K-S	0.9–1.8	96.5	K7	1,2,4
SU Aur	04 55 59.38	+30 34 01.5	Prz	3.0	3.5	G2	2,7
GW Ori	05 29 08.39	+11 52 12.7	Prz	...	27–29	G5	2,3
CR Cha	10 59 06.97	–77 01 40.3	Prz	...	30–44	K2	3,8
TW Hya	11 01 51.91	–34 42 17.0	Prz	9–10	194	K7	1,3,9,10
Glass I ^d	11 08 15.41	–77 33 53.5	Prz	2.5	22/1.4	K4	11–14
WW Cha	11 10 00.7	–76 34 59	Prz	0.3–0.8	66–67	K5	3,4,8,11
Hen 3-600 A	11 10 28.86	–37 32 04.8	K-S	10	12.5	M4	13,14
IRAS 14050-4109	14 08 10.3	–41 23 53	K-S	...	2.0	K5	13,15
RU Lup	15 56 42.31	–37 49 15.5	Prz,here	0.1–0.5	136–216	K7–M0	3,8,16
AS 205 NE	16 11 31.40	–18 38 24.5	Prz,here	0.1	154.6	K5	2,17
AS 205 SW	16 11 31.40	–18 38 24.5	Prz,here	<0.1	54.9	K5	2,17
DoAr 24E ^d	16 26 17.06	–24 20 21.6	Prz,here	1.5	5	K0	17,18
Haro 1-16	16 31 33.53	–24 27 33.4	Prz	...	59–76	K2–K3	2,8,18
AK Sco	16 54 44.85	–36 53 18.6	Prz	1.0	3–9	F5	3,13,19
S CrA NW	19 01 08.60	–36 57 20.0	Prz	3.0	73.	K3	13,17
S CrA SE	19 01 08.60	–36 57 20.0	Prz	1.0	61	MO	13,17
MWC 480	04 58 46.27	+29 50 37.0	K-S	5–6	18.3	A2–A3	1,20–23
UX Ori A	05 04 29.99	–03 47 14.3	vB	3–5	20.0	A2–A3	1,19,20–23
HD 37357	05 37 47.08	–06 42 30.2	vB	A0	22
HD 37806	05 41 02.29	–02 43 00.7	vB	6.3	...	B9–A2	22–24
HD 95881	11 01 57.62	–71 30 48.4	vB	...	21.1	A1–A2	21,22
HD 98922	11 22 31.67	–53 22 11.5	vB,here	...	27.9	B9	21,22
HD 101412	11 39 44.46	–60 10 27.7	vB	...	14–20	B9.5	13,21,22
HD 104237	12 00 05.08	–78 11 34.6	vB	2	24.3	A4	13,20–23,25
HD 142666	15 56 40.02	–22 01 40.0	vB	10	0.8–3	A7–A8	13,20–22
HD 144432	16 06 57.96	–27 43 09.8	vB	...	5–9	A7–F0	13,21–24
HD 150193	16 40 17.92	–23 53 45.2	vB	3–5	5	A0–A4	20–22,25
HD 163296	17 56 21.29	–21 57 21.9	vB,K-S,here	5	14.5	A0–A2	1,21–23,26
HD 179218	19 11 11.25	+15 47 15.6	K-S	0.1	18.2	B9–A0	21–23
WW Vul	19 25 58.75	+21 12 31.3	K-S	>10	18–24	B9–A3	3,4,20–22
HD 184761	19 34 58.97	+27 13 31.2	K-S	A8	27

REFERENCES. — (1) Thi et al. 2001; (2) Cohen & Kuhl 1979; (3) Reipurth et al. 1996; (4) Hartmann et al. 1998; (5) Strom et al. 1989; (6) Poncet et al. 1998; (7) Leveault 1988; (8) Appenzeller et al. 1983; (9) Webb et al. 1999; (10) Torres et al. 2003; (11) Lawson et al. 1996; (12) Gauvin & Strom 1992; (13) Gregorio-Hetem et al. 1992; (14) Chen et al. 1997; (15) Gregorio-Hetem & Hetem 2002; (16) Hughes et al. 1994; (17) Prato et al. 2003; (18) Bouvier & Appenzeller 1992; (19) Herbig & Bell 1988; (20) Natta et al. 1997; (21) Acke et al. 2005; (22) The et al. 1994; (23) van den Ancker et al. 1998; (24) Meeus et al. 2001; (25) van den Ancker et al. 1997; (26) Finkenzeller & Mundt 1984; (27) Miroshnichenko et al. 1999.

NOTE. — Sources in the top portion of the table are T Tauri stars; sources in the bottom portion are HAEBE stars.

^aThe RA and DEC quoted here were obtained from SIMBAD and do not necessarily represent the position of the referenced MIR spectroscopic observations.

^bReferences for silicate spectroscopy: vB = van Boekel et al. 2003; Prz = Przygodda et al. 2003; K-S = Kessler-Silacci et al. 2005; here = this paper.

^cAll H α lines are in emission

^dThis source is a binary that is unresolved in the referenced MIR spectroscopic observations. Stellar/disk parameters quoted from the literature include both sources.

composition and whether DHS or Mie models are used (see bottom panel of Figure 9a).

The observed trend is best fit with models of amorphous pyroxene/olivine mixtures. Models of pure amorphous olivines calculated using DHS are inconsistent with the observations. These models possess generally larger $S_{11.3\text{-to-}S_{9.8}}$ ratios than the data, particularly for strong features. Mie models of pure amorphous olivines fit the data much better, but begin to deviate from observations near $S_{peak}^{10\mu m} \approx 2$. The slope of the observed trend can be best matched using mixtures with 30% amorphous olivines and 70% amorphous pyroxenes. This pyroxene fraction is much larger than that in-

ferred for diffuse ISM grains in the galactic center (15.1% pyroxene; Kemper et al. 2004), indicating a substantial conversion of olivines to pyroxenes in young stellar environments. Enhanced pyroxene-to-olivine abundances were previously observed toward high-mass protostars with ISO and may be explained by He⁺ sputtering in high-velocity shocks (Demyk et al. 2001, and references therein).

Models of olivine-pyroxene mixtures fit the data best for homogeneous filled spheres (Mie) and hollow spheres (DHS), but do not fit equally well for all grain sizes (peak strengths). For the weakest 10 μm features ($S_{peak}^{10\mu m} \leq 1.75$), hollow sphere models indicate grain sizes of up to 1.3 times those of

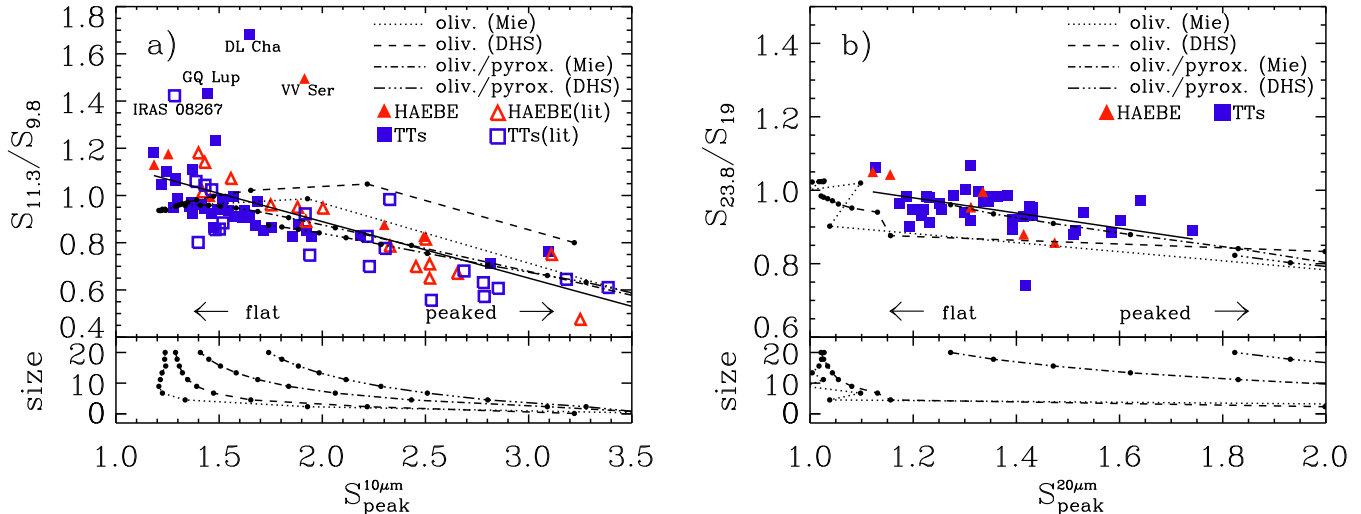


FIG. 9.— Shape and strength of the *a*) 10 μm and *b*) 20 μm silicate features. The shapes of the features (probed by the normalized flux ratios, $S_{11.3}/S_{9.8}$ and $S_{23.8}/S_{19}$) are plotted versus the feature strengths ($S_{10\mu m}^{peak}$ and $S_{20\mu m}^{peak}$) in the top panels of each figure. The data observed in this study are denoted by filled squares (TTs) and filled triangles (HAEBE). Data for 10 μm silicate features from the literature (van Boekel et al. 2003; Przygodda et al. 2003; Kessler-Silacci et al. 2005) are always represented by open symbols. The black line in *a*) indicates the correlation found for the 10 μm features including all data, and follows the relation, $y = A + Bx$, where $A = 1.37 \pm 0.05$ and $B = -0.24 \pm 0.03$, with a correlation coefficient of $r = -0.7$. The 20 μm features also show a correlation ($r = -0.5$), with $A = 1.23 \pm 0.08$ and $B = -0.21 \pm 0.06$. Models of amorphous olivines, pyroxenes and mixtures of the two for various grain shapes are overlaid as dashed-dotted lines connecting points representing grains with a linear size distribution between 0.1 and 20 μm (see text for details). The bottom panels of each figure show the grain size vs. peak strength for the models.

homogeneous spheres for features of the same strength. Both mixture models indicate that the largest changes in the shape of the feature occur over a small range of grain sizes, from approximately 1–3 μm , with exact values depending on the model used. For the weakest silicate features ($S_{10\mu m}^{peak} \leq 1.7$), large changes in grain size result in only small variations in the strength/shape of the silicate feature. Therefore, it becomes increasingly difficult to determine exact grain sizes for the weakest silicate features.

The data discussed above cannot be explained purely by size variations, and in some cases can indeed be attributed to crystalline silicates and/or PAH emission. For the largest grain sizes, Figure 9a shows several spectra with 11.3-to-9.8 μm ratios that consistently lie above the modeled ratios. These data may indicate the presence of crystalline forsterite or PAH emission in the 11.2–11.3 μm region. For a cutoff at $S_{11.3}/S_{9.8} = 1.0$, we find that 13 sources in our sample satisfy this criterion, and thus require emission near 11.3 μm that is in excess above models of amorphous olivines/pyroxenes, indicating that the features arise from crystalline silicates or PAHs. These sources are marked with a “Y” in the column 3 of Table 2. Of these 13 sources, 4 show clear evidence of crystalline silicate emission at $\lambda > 25 \mu\text{m}$ (DoAr 24E, GY 23, HD 98922 and DL Cha). Clear evidence for PAH emission features in the SL spectra can be seen in 3 additional sources (LkH α 330, IRAS 03446+3254, Haro 1-17 and HD 135344). The spectra of 3 more sources (VSSG1, LkH α 327, and RR Tau) show evidence of both PAH and crystalline silicate features. The remaining 3 sources with $S_{11.3}/S_{9.8} > 1.0$ (T Cha, SR 21, and HD 135344) display narrow isolated 11.3 μm emission and have very simple spectra that show only shallow $\sim 20 \mu\text{m}$ silicate emission. This likely indicates that the 11.3 μm features in these 3 spectra arise from PAH, and not crystalline silicate, emission. Therefore, for all of the spectra with $S_{11.3}/S_{9.8} > 1.0$, the additional flux at 11.3 μm can indeed be explained by crystalline silicate and/or PAH emis-

sion. The nature of the 11.3 μm features and relationship to PAH emission will be discussed more thoroughly in Geers et al. (in prep.). Aside from the spectra with $S_{11.3}/S_{9.8} > 1.0$, the data presented in Figure 9a are consistent with grain size variations.

The 20 μm features show a shape-strength trend which is very similar to that seen for the 10 μm features (Figure 9b). Here we use the ratio of the flux at 23.8 to 19 μm , again the peaks of the most prominent amorphous and crystalline silicate features, as a proxy for the feature shape. This plot includes only c2d data, as continuum normalized ISO data were not available. The paucity of spectra with strong 20 μm features may be related to the prominence of weak, flat 10 μm features in the c2d sample, indicating large grain sizes. Although the sample size (and range in peak strength) is smaller for the 20 μm features, the shape-strength trend is still prominent. This trend possesses a similar slope and y-intercept to that seen for the 10 μm features and is again most closely matched with the Mie model of an olivine/pyroxene mixture, which agrees to within $S_{23.8}/S_{19} = 0.01$, or $\sim 1\%$. There appears to be little difference in grain composition between grains being probed by the 10 and 20 μm features.

All of the 20 μm features are consistent with models of amorphous olivine/pyroxene mixtures of sizes between 0.1 and 20 μm , with no deviations indicative of strong crystalline features. A similar fit is obtained for the Mie and DHS models of the olivine/pyroxene mixture, but for the DHS models much larger grain sizes ($a > 20 \mu\text{m}$) are needed. The data are also consistent with DHS and Mie models of amorphous olivines (to within $S_{23.8}/S_{19} = 0.08$, or $\sim 8\%$), for much smaller grain sizes ($a \leq 5 \mu\text{m}$). This makes exact grain-size determination difficult. Furthermore, a large scatter in the modeled data points can be seen for $S_{20\mu m}^{peak} < 1.1$ due to difficulties in fitting the continuum for such weak features. This prevents identification of small deviations in feature shape of between the models and data for large grain sizes (as were

TABLE 5
MODEL PARAMETERS FOR FIGURE 10.

Panel	Parameter	Variables	Range
b	size distribution ^a	a_{min}	0.01–3.0 μm
		a_{max}	10–100 μm
		p	4.5–2.5
c	sizes for 10 vs 20 μm	p	4.5–2.5
		a_{min}^{10}	0.1, 1.0 μm
		a_{min}^{20}	(0.1–20) \times 0.1 μm
		a_{min}^{30}	(0.5–3) \times 1.0 μm
d	composition	$a_{min}^{10} = a_{min}^{20}$	0.01–3.0 μm
		olivine:carbon	100:0–50:50
		olivine:pyroxene	100:0–0:100
e	crystallinity	$a_{min}^{10} = a_{min}^{20}$	0.01–3.0 μm
		olivine:forsterite	100:0–0:100
		olivine:enstatite	100:0–0:100
f	porosity	$a_{min}^{10} = a_{min}^{20}$	0.01–3.0 μm
		a_{min}^{20}	100:0–20:80
		a_{min}^{vacuum}	100:0–20:80

^aUsing a differential grain size distribution of $dn(a) \propto a^{-p} da$ where the absorption efficiency is defined as $\langle Q_{abs} \rangle = \int_{a_{min}}^{a_{max}} Q_{abs} dn(a) / \int_{a_{min}}^{a_{max}} dn(a)$.

seen for the 10 μm features). However, larger deviations from the models are not seen. Thus, although there is evidence in some individual spectra for crystalline silicate features, the entire trend is consistent with amorphous olivine/pyroxene mixtures with source-to-source size variations.

For the 48 sources observed in this study, the 10 and 20 μm features both exhibit strength-shape trends consistent with source-to-source grain-size variations, with most of the observed features similar to models of grains with sizes much larger than that of the ISM ($a \gg 0.1 \mu\text{m}$). This indicates that grain growth must occur quickly in these disks. Furthermore, as the observed features arise from silicate emission in the disk surface layers, and the largest grains will gravitationally settle to the disk midplane, the emitting grains likely represent the low-size tail of the silicate grain size distribution within the disk. This effect is enhanced by the fact that larger grains have weaker silicate emission features.

5.2. 10 vs. 20 μm feature strengths

One of the most interesting aspects of this sample is a set of sources with very strong $S_{peak}^{10\mu\text{m}}$ but weak $S_{peak}^{20\mu\text{m}}$. These “outliers” can be clearly seen in a plot of the strengths of the 10 and 20 μm features in the observed spectra (Figure 10; Table ??). The feature strengths appear to be correlated over the entire sample ($r = 0.36$, 96% probability of correlation). However, examination of Figure 10a reveals that the bulk of the data is clustered around $S_{peak}^{20\mu\text{m}} \approx 1.3$ and $S_{peak}^{10\mu\text{m}} \approx 1.5$ and ~ 11 outliers have 10 μm and 20 μm features with very different strengths. Furthermore, most of these outliers have strong 10 μm features ($S_{peak}^{10\mu\text{m}} > 2$) and weak 20 μm features ($S_{peak}^{20\mu\text{m}} < 1.6$). No sources in our sample have strong 10 μm features and equally strong 20 μm features. One may expect weak 20 μm features to be more abundant as most sources show weak 10 μm features (cf. Figure 9a) and grain growth is occurring quickly in these disks. However, the fact that there are no sources with strong 20 μm features and weak 10 μm features is significant.

In order to interpret the distribution of peak strengths in the observed spectra, we examine the effect of a variety of grain parameters on the strengths of the 10 and 20 μm fea-

tures. Factors affecting silicate feature strengths include, but are not limited to, the grain size distribution, relative sizes of grains emitting at 10 and 20 μm , grain composition, crystallinity, and porosity. We attempt to assess the influence of each of these parameters in panels b–f of Figure 10 and §5.2.1–5.2.4 for models of normalized Q_{abs} calculated as described in §4.2.

5.2.1. Grain size distributions

The effects of grain size are explored by modeling opacities for a set of grains with a differential grain size distribution $dn(a) \propto a^{-p} da$, and varying the minimum grain size a_{min} , maximum grain size a_{max} , and power-law index p , as shown in Figure 10b. All three parameters have very similar effects; increasing a_{min} or a_{max} or decreasing p results in more large grains and reduces both the 10 and 20 μm feature strengths, but does not affect the ratio of the two. Thus, variation of the grain size distribution cannot account for the extreme 10-to-20 μm ratios of the outliers in Figure 10a. The bulk of the observed data set is centered around 10 and 20 μm feature strengths similar to that of a grain size distribution with $a_{min} = 1.0 \mu\text{m}$, $a_{max} = 100 \mu\text{m}$, and power-law index $p = 3.5$.

The emission at 10 and 20 μm likely comes from different populations of grains. This is a simple consequence of the temperature dependence of the emission as a function of wavelength (e.g., emission at 20 μm can arise from colder grains than emission at 10 μm). We therefore expect the contribution of a particular grain to the 10 and 20 μm features to depend on the location of the grain. In order to determine the relative contribution of grains from different radii to the 10 and 20 μm features, we perform an exercise using a simple two-layer model (CGPLUS, Dullemond et al. 2001; Chiang & Goldreich 1997) to calculate the cumulative disk flux as a function of radius at 10 and 20 μm for a typical T Tauri star. Figure 11 shows that the radii probed by the 10 and 20 μm silicate features can indeed be quite different, with the 20 μm feature probing radii up to 10 times those probed by the 10 μm feature.

In Figure 10c, the relationship between the sizes of the grains emitting at 10 and 20 μm is explored. We vary a_{min} for the models of the 20 μm feature and keeping a_{max} , p , and a_{min} for the models of the 10 μm feature constant. The entire distribution of the data can be reproduced by these models. Most data correspond to $a_{min}^{10\mu\text{m}} = 1 \mu\text{m}$ and $a_{min}^{20\mu\text{m}} = 0.1–3 \mu\text{m}$, but the data in the right side of Figure 10c require large differences between the sizes of grains emitting at 10 and 20 μm ($a_{min}^{10\mu\text{m}} = 0.1 \mu\text{m}$, $a_{min}^{20\mu\text{m}} = 2–3 \mu\text{m}$).

The 10 and 20 μm features are clearly probing different dust populations. The bulk of the data can be reproduced by models of 1.0 μm grains, indicating significant growth in these disks compared to the ISM. Although the data are clustered centered around the dashed lines that denote equal grain sizes for 10 and 20 μm emission, many spectra can be better represented by much larger grains emitting at 20 μm than at 10 μm . This may be explained, if the emission is optically thin, by a difference in the $\tau = 1$ surface depth as a function of wavelength of the emission; 20 μm features probe a deeper layer of the disk where grain sizes are likely larger due to larger density and dust settling. One would also expect, however, that dust at larger radii (and lower temperature), which is likely smaller due to decreased densities, contributes more to the 20 μm feature than the 10 μm feature. There is thus a com-

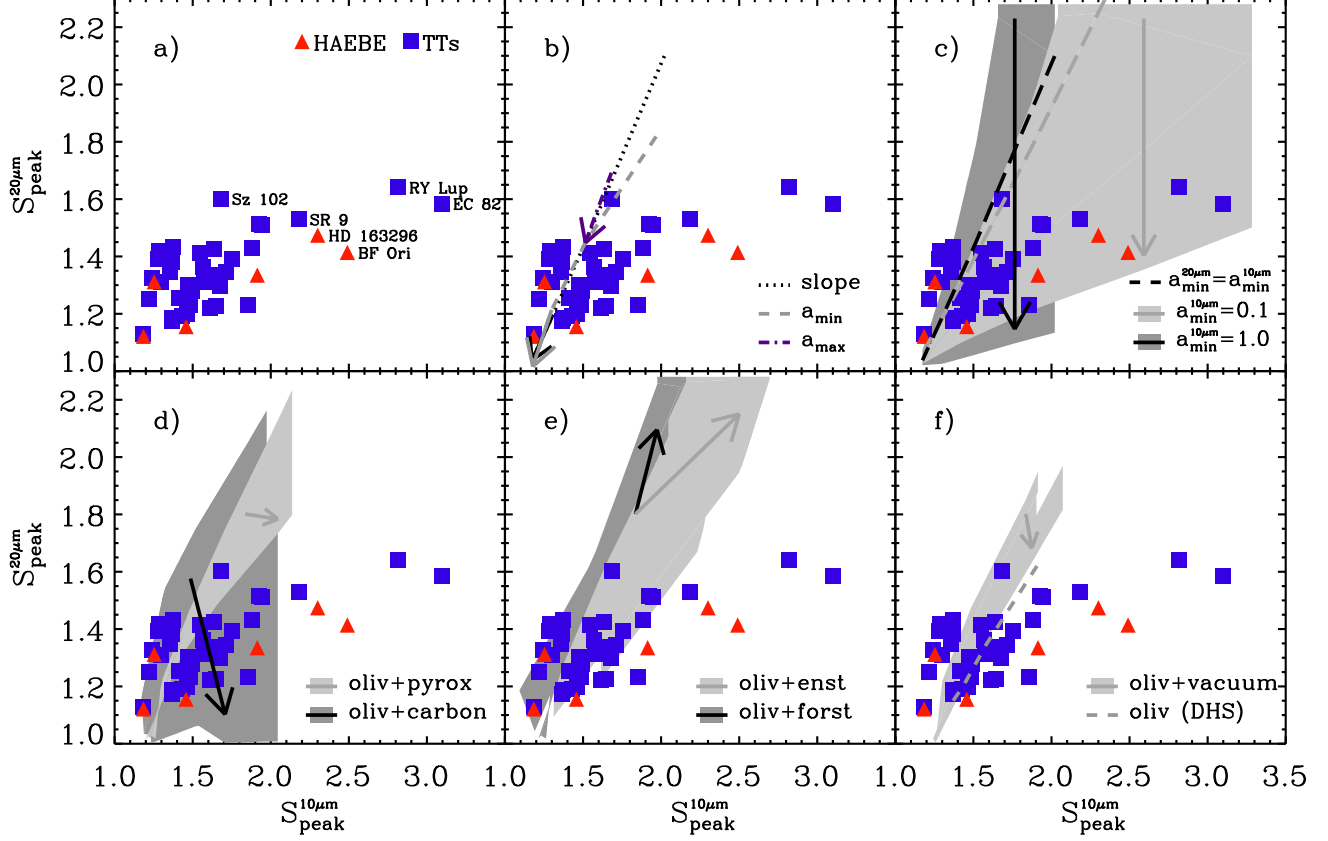


FIG. 10.— Relative strengths of the 20 versus 10 μm features. Models are overplotted showing variations in *b*) grain size distribution, *c*) ratios of grain sizes emitting at 10 and 20 μm , *d*) grain composition, *e*) crystallinity, and *f*) porosity. The reference opacities are calculated via Mie theory for pure olivine grains with differential grain size distributions with $a_{\min} = 1.0\mu\text{m}$, $a_{\max} = 100\mu\text{m}$, and power-law index $p = -3.5$ for both the 10 and 20 μm features. Arrows in panel *b* indicate the direction of increasing slope p , a_{\min} and a_{\max} . Gray shaded regions in *c*) indicate the range in 10 and 20 μm feature strengths covered by variations in $a_{\min}^{20\mu\text{m}}$ with $a_{\min}^{10\mu\text{m}} = 0.1\mu\text{m}$ and $a_{\min}^{10\mu\text{m}} = 1.0\mu\text{m}$. Arrows in panel *c* indicate the direction of increasing 10-to-20 μm grain size ratios over the gray shaded regions. Gray shaded regions in *d*–*f* indicate the range in 10 and 20 μm feature strengths covered by variations in $x/\text{olivine}$ ratios, where x is *d*) pyroxene or amorphous carbon, *e*) forsterite or enstatite, and *f*) vacuum for grains of constant size. Arrows in *d*–*f* indicate the direction of increasing $x/\text{olivine}$ ratios. Symbols are defined as in Figure 9.

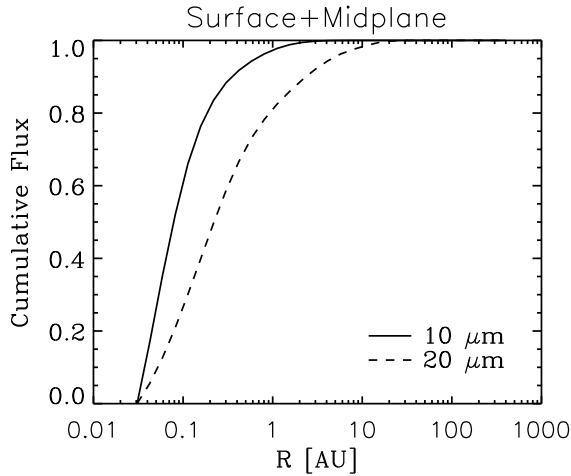


FIG. 11.— Cumulative flux at 10 μm (solid line) and at 20 μm (dashed line) as a function of radius. Fluxes are calculated using the CGPLUS model (Dullemond et al. 2001) for a disk around a T Tauri star with $T_* = 4000\text{ K}$, $L_* = 0.58 L_\odot$ containing olivine grains of a differential grain size distribution with $a_{\min} = 1\mu\text{m}$, $a_{\max} = 100\mu\text{m}$ and $p = -3.5$. 95% of the 10 μm flux comes from within $\sim 1\text{ AU}$, while 95% of the 20 μm flux comes from within $\sim 10\text{ AU}$.

peting effect between the disk height and radius being probed. This may explain why most of the data points are centered around the dashed lines that denote equal grain sizes for 10 and 20 μm emission. In the case of the outliers, enhanced dust settling may make the disk height differential between dust probed by the two features more important than the difference in radius.

5.2.2. Grain composition and crystallinity

Grain composition and crystallinity also affect the strengths of the silicate emission features, resulting in ranges of peak strengths that are very similar to those produced by varying the grain sizes (with $a_{\min}^{10\mu\text{m}} = a_{\min}^{20\mu\text{m}}$). Thus, effects of grain-size variation, composition and crystallinity are difficult to disentangle using 10-to-20 μm flux ratios.

In Figure 10d, we vary the percentage of amorphous pyroxene and amorphous carbon relative to amorphous olivine. To simplify matters, we use the same composition and grain sizes for the grains emitting at 10 and 20 μm . Increasing the pyroxene-to-olivine fraction has the largest effects for small grains ($< 1.0\mu\text{m}$), resulting in an increased 10 μm feature strength and roughly constant 20 μm feature strength (as seen previously in Figure 9). Increasing the carbon-to-olivine fraction has an even larger effect on grains of small sizes, with a

larger effect on the 20 μm feature than the 10 μm feature, as the peak-to-continuum ratio is decreased due to an increase in the effective “continuum.”

Variations in crystallinity (using DHS models) also result in the same range of peak strengths, but highly crystalline grains can produce features with the same peak strengths at smaller grain sizes (Figure 10e). When the fraction of forsterite or enstatite is less than $\sim 50\%$, the feature strengths remain very similar to amorphous olivine. Beyond a crystalline fraction of $\sim 50\%$, the strong and narrow crystalline emission features begin to dominate and the strengths of the peak emission in the 10 and 20 μm regions appear to increase dramatically for the same grain size distribution. For models of $>50\%$ crystalline forsterite and enstatite, the gray shading in Figure 10e extends far beyond the plotted range of the y-axis ($S_{peak}^{20\mu\text{m}} \gg 2.28$). Thus, for primarily crystalline grains, grain size distributions with $a_{min} \leq 2.0 \mu\text{m}$ can account for the entire gray area shown.

Differing composition and crystallinity can account for the 10 and 20 μm ratios of the bulk of the observed spectra, but not the outliers. Additionally, the 10 and 20 μm ratios of models of varying grain composition and crystallinity encompass ranges in which no observational data lie. In particular, spectra showing weak 10 μm features ($S_{peak}^{10\mu\text{m}} > 1.7$) and strong 20 μm features can be easily produced with models of small-sized ($a_{min} < 1.0 \mu\text{m}$) amorphous silicate/carbonaceous grains or moderately-sized ($a_{min} < 3.0 \mu\text{m}$) crystalline silicate grains, but they are not seen in the *c2d* sample. These absences confirm the idea that the 20 μm feature probes regions of larger grain size than does the 10 μm feature, irrespective of grain composition and crystallinity.

5.2.3. Dust porosity

Finally, in Figure 10f we explore the effects of grain opacity by increasing the vacuum fraction of a set of olivine grains and by using the distribution of hollow spheres method (DHS). In both cases, we integrate over a grain size distribution as in Figure 10d–e. The primary difference between the two methods is that the opacities calculated with DHS are the average of a set of hollow spheres of varying vacuum fractions for a given mass, which is translated to grain size. The Q_{abs} are then integrated over a grain size distribution. For the olivine+vacuum grains, the opacities and Q_{abs} are calculated and integrated over grain size for each volume fraction individually. The variation over vacuum fraction (light gray in Figure 10f) does not have a large effect on the 10-to-20 μm ratio and is consistent with the DHS 10 and 20 μm strengths and variation with a_{min} . Variations in dust porosity can only explain a fraction of the bulk of the sample, which overlaps with the regions covered by models of varying grain composition, and cannot explain the outliers. Thus it is not necessary to consider porosity to explain the observed 10 and 20 μm feature strengths.

6. GRAIN GROWTH AND STELLAR/DISK PROPERTIES

In order to evaluate the dependence of the strength-shape trend noted in §5 on stellar and disk parameters, we plot the 10 μm shape versus strength again in Figures 12a–c, color-coded by spectral type, stellar age, and $\text{H}\alpha$ equivalent width (for TTs only). Stellar/disk parameters for each source observed in this study (*c2d*) were collected from the literature and are shown in Table 1. Stellar/disk parameters for 10 μm data obtained from van Boekel et al. (2003), Przygodda et al.

(2003), and Kessler-Silacci et al. (2005) (*lit*) are shown in Table 4. We evaluate the probability that the sets of spectral type, stellar age or $\text{H}\alpha$ equivalent width bins are drawn from the same distribution on the 10 μm feature shape-strength relation shown in Figure 9a by evaluating the two-sided Kolmogorov-Smirnov statistic (D)¹⁴ for each stellar/disk parameter. As we are evaluating the dependence of the strength-shape trend on stellar/disk parameters, we use only the sources with $S_{11.3}/S_{9.8} < 1.0$, thus removing sources with substantial emission from crystalline silicates and/or PAHs. Some stellar/disk parameters are not available in the literature, and therefore not all sources are included in Figures 12a, b, and c.

6.1. Spectral Type

As the data in our sample (filled symbols) appear to be consistent with the largest silicate grain sizes, and probe disks around primarily K and M stars, we first looked for connections between grain size and spectral type. We divide the sample by spectral type into four groups: 1) A/B, 2) F/G, 3) K and 4) M. The A and B stars and F and G stars were combined into single groups as few stars of each type were observed. The Kolmogorov-Smirnov (K-S) test is used to compare two arrays of data values and the process is repeated for each combination of groups 1 through 4. In general, there appears to be a dependence on spectral type, with A/B stars being clustered toward the middle and lower right of the 10 μm feature strength-shape trend and M stars being more clustered toward the upper left of Figure 12. This can be more easily seen in Figure 13, where histograms of the 10 μm shape-to-strength ratio for A/B stars and M stars are compared. The population of A/B stars peaks at ratios near 0.1 and decreases for larger ratios, while only a few M stars have shape-to-strength ratios near 0.1 and the population increases for larger ratios to peak near 0.5–0.6.

Although it appears that 10 μm silicate emission may be different in A/B stars versus M stars, a larger data set is needed to confirm this result. The calculated probabilities that these groups are drawn from the same distribution range from 15% ($D = 0.29$) for spectral types A/B and M to 98% ($D = 0.17$) for spectral types A/B and F/G. Objects that are close in spectral type, in subsequent groups (e.g., 1 vs. 2, 2 vs. 3), have large probabilities (69–98%) of being drawn from the same distribution. Groups with larger differences in spectral type (e.g., 1 vs. 3, 2 vs. 4) have smaller probabilities (15–50%). Of all these comparisons, however, only the K-S test for group 1 vs. 4 (A/B vs. M) indicates a low enough probability ($\leq 20\%$, Press et al. 1992) to suggest that the differences in the populations are statistically significant. Furthermore, the number of objects in each group is still quite low (13 A/B stars, 4 F/G stars, 24 K stars, and 15 M stars) and the spectral types typically have errors on the order of 3 subclasses.

The dependence of the strength-shape trend with spectral type may be explained in terms of the disk temperature and density structure. If we assume that the 10 μm feature always probes grains of roughly the same temperature, then the radius being probed by the 10 μm emission will change as a function of the temperature structure of the disk. The disk temperature

¹⁴ The two-sided Kolmogorov-Smirnov statistic is the difference between the cumulative distribution function (CDF) of two sets of data and is calculated using **KSTWO** (from Numerical Recipes; Press et al. 1992).

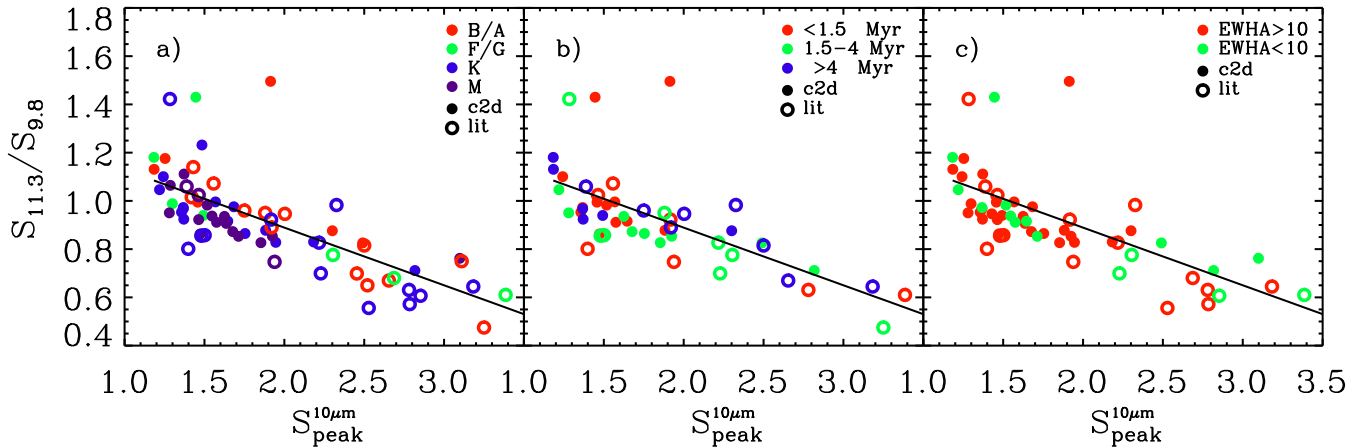


FIG. 12.— Shape and strength of the $10\ \mu\text{m}$ silicate features. The shape of the feature ($S_{11.3}/S_{9.8}$) is plotted versus the feature strength ($S_{10\mu\text{m}}^{\text{peak}}$) in all panels. The points are color-coded by *a*) spectral type, *b*) age and *c*) $H\alpha$ equivalent width. Silicate features from the literature (van Boekel et al. 2003; Przygodna et al. 2003; Kessler-Silacci et al. 2005) are always represented by open symbols. The black line in all panels indicates the correlation found for the $10\ \mu\text{m}$ features shown in Figure 9a including all observations. This trend is not strongly dependent on $H\alpha$ EW or age, but may be related to spectral type.

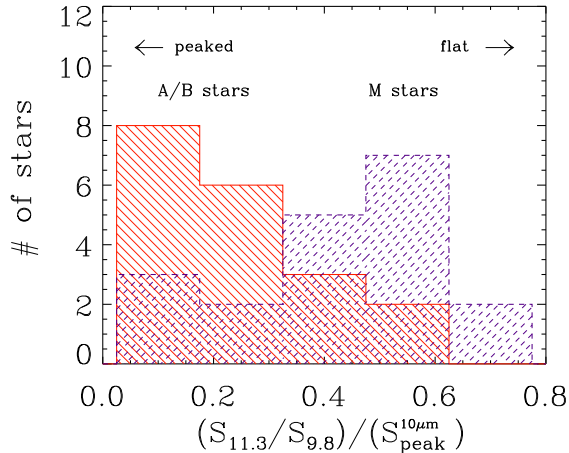


FIG. 13.— Histogram of the $10\ \mu\text{m}$ feature shape-to-strength ratios for the A/B and M stars shown in Figure 12a. Spectra of A and B stars show more centrally peaked $10\ \mu\text{m}$ features, lying in the middle and left of Figure 12a, while spectra of M stars show primarily flattened features, lying in the upper left of Figure 12a. The bin widths are 0.1 in units of $(S_{11.3}/S_{9.8})/(S_{10\mu\text{m}}^{\text{peak}})$.

$T(R)$ varies as a function of radius as

$$T(R) = \alpha^{1/4} \sqrt{\frac{R_*}{R}} T_*,$$

(from Dullemond & Dominik 2005), where α is the disk flaring angle and R_* and T_* are the stellar radius and temperature. R is the radius corresponding to temperature $T(R)$, in this case the dominant radius being probed by the silicate emission feature, which we will call R_{sil} . Assuming that $T(R_{\text{sil}})$ and α are constant over the entire disk sample, and using typical values of R_* and T_* for A/B and M stars, $R_{\text{sil,A/B}}/R_{\text{sil,M}} \approx 10$ –25. So the radius probed by the $10\ \mu\text{m}$ emission feature is quite different for stars of spectral types A/B and M. Furthermore, the density generally increases with decreasing radius and grain growth increases at higher density, while dust settling decreases at higher density. Thus, the combination of faster grain growth and slower dust settling at smaller radii

could lead to the larger grains that we see in M stars versus A/B stars. Although this simple theory is consistent with the observed correlation of grain size with spectral type, several other spectral-type dependent factors (e.g., X-rays, UV radiation, stellar/disk winds, etc.) likely influence grain size in these disks.

6.2. Age

Although one might expect grain growth and crystallization to occur over time, as the disk matures, we see no clear relationship between the strength-shape trend and stellar age (Figure 12b). The ages for our sample are culled from the literature and range from 0.5 to 6 Myr with errors of up to a few Myr (i.e., Hillenbrand & White 2004). We therefore divide up the sample into three approximately equally sized groups: stars with ages of 1) < 1.5 Myr, 2) 1.5 – 4 Myr, and 3) > 4 Myr, and follow a similar method as described above for the analysis of spectral type. The strength-shape trend does not appear to be strongly related to the age of the star (Figure 12b), with probabilities of $> 47\%$ that all three groups are drawn from the same distribution. However, this analysis would be more conclusive for stars within one cluster with a well defined age, for which relative ages could be more accurately determined. With the available ages, these results indicate that the stellar age of PMS stars is not directly related to the state of the small, μm -sized grains in these disks.

In addition to the difficulties in determining the disk age, the lack of an age dependence of the shape-strength trend can be understood when grain fragmentation and disk turbulence are considered. Dullemond & Dominik (2005) find that in models including only basic coagulation mechanisms grain growth occurs very quickly, such that the SEDs show much weaker IR excess (even at young ages of 1 Myr) than do disks around most classical TTs. The settling of small grains, removing them from the disk surface, occurs over even faster time scales. The lack of sources with strongly peaked $10\ \mu\text{m}$ features (and therefore small grains) in the substantial sample observed here is consistent with this fast timescale for grain growth (to $1\ \mu\text{m}$ sizes). The presence of strongly peaked $10\ \mu\text{m}$ features in some sources (particularly in the *lit* sample) may be indicative of the replenishment of

small grains in disk surface layers through mechanisms such as fragmentation and/or turbulent mixing. (Some amount of large grains will also be mixed into disk surface layers). The models presented in Dullemond & Dominik (2005) suggest that such mechanisms may allow disk systems to maintain quasi-stationary grain size distributions, with grain growth and small-grain replenishment rates in equilibrium for long periods of time (≥ 1 Myr). Thus the typical grain sizes found in disks around pre-main sequence stars are likely not to be directly related to disk age, but indicative of a number of other factors, such as the strength of the turbulence and the gas mass in the disk.

6.3. Accretion

We also do not see a correlation of the strength-shape trend with the equivalent width of the $H\alpha$ emission lines ($H\alpha EW$), probing disk evolution (Figure 12c). The $H\alpha$ equivalent width is a tracer of active stellar accretion from the inner disk. Thus clearing of the inner disk will result in lower $H\alpha EW$. In Figure 12c, we separate the TTs in our sample into two groups using the equivalent width of $H\alpha$: 35 classical T Tauri stars (cTTs; $H\alpha EW > 10 \text{ \AA}$) and 14 weak-lined T Tauri stars (wTTs; $H\alpha EW < 10 \text{ \AA}$). Although there is no clear observational evidence that cTTs are progenitors to wTTs, wTTs are often described as cTTs in which the inner disk has dissipated. Therefore, we might expect that the clearing of the inner disk, and thus the transition between the classical and weak-line T Tauri star phases, would be related to grain growth and the $10 \mu\text{m}$ feature strength-shape trend. We find that there is a high probability ($\sim 70\%$) that the two groups are drawn from the same distribution, however, indicating that there is no clear relationship between $H\alpha EW$ and grain growth in these disks. This indicates that either $H\alpha EW$ is not a good probe of the disk evolutionary state or stellar accretion rate or that grain growth is not related to these quantities. We also note that $H\alpha$ emission can be quite variable and the values used here are time averages, using the full range of observed $H\alpha EW$ as error bars. The relation between $H\alpha EW$ and silicate feature shape-strength would more precisely tested with simultaneous MIR and optical spectroscopy.

7. CONCLUSIONS

Spectra in the $\sim 5\text{--}35 \mu\text{m}$ region have been obtained for disks around 40 TTs and 7 HAEBE stars using the Spitzer Space Telescope, as a subset of the c2d IRS survey. This is the first significant sample of T Tauri stars for which both $10 \mu\text{m}$ and $20 \mu\text{m}$ features are available. Broad silicate features at $10 \mu\text{m}$ and $20 \mu\text{m}$, similar to emission from amorphous silicates, are prominent toward the observed sample of TTs and HAEBE stars. Emission features from crystalline silicates are also evident in the observed spectra, with the most prominent features visible in the $33\text{--}36 \mu\text{m}$ region.

We performed a statistical analysis of the shapes and strengths of the $10 \mu\text{m}$ and $20 \mu\text{m}$ features and find the following:

- If the full IRS spectra are considered, the data are most consistent with source-to-source variations in grain size, with the bulk of the sources in our sample indicating sizes of $1 \mu\text{m}$ or greater. This and the lack of strongly peaked $10 \mu\text{m}$ sources in our sample of 40

sources is consistent with fast grain growth (from $0.1\text{--}1.0 \mu\text{m}$ sizes) in the surfaces of these disks.

- Long wavelength ($33\text{--}36 \mu\text{m}$) crystalline silicate features are seen toward \sim half of the TTs disks in our sample. This indicates that significant dust processing is also occurring in these disks. Only 13 of these spectra also exhibit $11.3\text{--}9.8 \mu\text{m}$ ratios that cannot be reproduced by models of amorphous silicates, suggesting that the degree of crystallinity deduced from the $10 \mu\text{m}$ region alone is underestimated.
- A subset of the observed spectra have particularly large $10\text{--}20 \mu\text{m}$ ratios, which can only be reproduced with much smaller grains emitting at $10 \mu\text{m}$ ($a_{min} = 0.1 \mu\text{m}$) than at $20 \mu\text{m}$ ($a_{min} = 2\text{--}3 \mu\text{m}$). This can be explained if the $20 \mu\text{m}$ emission arises from deeper in the disk than the $10 \mu\text{m}$ emission in disks where dust settling has occurred.
- The $10 \mu\text{m}$ feature strength vs. shape trend *is not* correlated with age or disk evolutionary state ($H\alpha EW$). This suggests the importance of turbulence and the regeneration of small (μm -sized) grains on the disk surface.
- The $10 \mu\text{m}$ feature strength vs. shape trend *is* related to spectral type, with M stars showing significantly flatter silicate features (larger grain sizes) than those of A/B stars. This may be related to a difference in the radius probed by the emission, which should increase as a function of the disk temperature, and thus stellar luminosity. However, the observed correlation could also be indicative of other spectral-type dependent factors (e.g., X-rays, UV radiation, stellar/disk winds, etc.).

As the observed features arise from silicate emission in the disk surface layers, and the largest grains will gravitationally settle to the disk midplane, the emitting grains likely represent the small-size tail of the silicate grain size distribution within the disk. This simple picture of grain growth and settling is complicated by vertical mixing, which can bring both large and small grains back to the disk surface, and fragmentation, which results in the replenishment of small grains throughout the disk. Comparisons with probes of grain size in the disk midplane and inner disk clearing, as well as probes of disk turbulence and gas-dust interactions, are vital to understanding the results presented here in the context of planet formation.

Support for this work, part of the Spitzer Space Telescope Legacy Science Program, was provided by NASA through Contract Numbers 1256316, 1224608 and 1230780 issued by the Jet Propulsion Laboratory, California Institute of Technology under NASA contract 1407. Astrochemistry in Leiden is supported by a NWO Spinoza and NOVA grant, and by the European Research Training Network "The Origin of Planetary Systems" (PLANETS, contract number HPRN-CT-2002-00308). The authors would like to thank Michiel Min for communicating his results on DHS and Jeroen Bouwman, Thomas Henning, Roy van Boekel, Rens Waters, Antonella Natta, David Koerner and the ApJ referee for helpful comments and suggestions.

REFERENCES

- Alcala, J. M., Krautter, J., Schmitt, J. H. M. M., Covino, E., Wichmann, R., & Mundt, R. 1995, *A&AS*, 114, 109
- Appenzeller, I., Krautter, J., & Jankovics, I. 1983, *A&AS*, 53, 291
- Bouvier, J. & Appenzeller, I. 1992, *A&AS*, 92, 481
- Bouwman, J., Meeus, G., de Koter, A., Hony, S., Dominik, C., & Waters, L. B. F. M. 2001, *A&A*, 375, 950
- Bradley, J. 2003, *LNP Vol. 609: Astromineralogy*. Edited by T. K. Henning., 609, 217
- Chen, H., Grenfell, T. G., Myers, P. C., & Hughes, J. D. 1997, *ApJ*, 478, 295
- Chiang, E. I. & Goldreich, P. 1997, *ApJ*, 490, 368
- Chiang, E. I., Joun, M. K., Creech-Eakman, M. J., Qi, C., Kessler, J. E., Blake, G. A., & van Dishoeck, E. F. 2001, *ApJ*, 547, 1077
- Cohen, M. & Kuhl, L. V. 1979, *ApJS*, 41, 743
- D'Alessio, P., Calvet, N., Hartmann, L., Lizano, S., & Cantó, J. 1999, *ApJ*, 527, 893
- D'Alessio, P., Hartmann, L., Calvet, N., Franco-Hernández, R., Forrest, W. J., Sargent, B., Furlan, E., Uchida, K., Green, J. D., Watson, D. M., Chen, C. H., Kemper, F., Sloan, G. C., & Najita, J. 2005, *ApJ*, 621, 461
- Demyk, K., Carrez, P., Leroux, H., Cordier, P., Jones, A. P., Borg, J., Quirico, E., Raynal, P. I., & d'Hendecourt, L. 2001, *A&A*, 368, L38
- Dorschner, J., Begemann, B., Henning, T., Jaeger, C., & Mutschke, H. 1995, *A&A*, 300, 503
- Dullemond, C. P. & Dominik, C. 2004, *A&A*, 417, 159
- . 2005, *A&A*, 434, 971
- Dullemond, C. P., Dominik, C., & Natta, A. 2001, *ApJ*, 560, 957
- Dunkin, S. K., Barlow, M. J., & Ryan, S. G. 1997, *MNRAS*, 286, 604
- Evans, N. J., Allen, L. E., Blake, G. A., Boogert, A. C. A., Bourke, T., Harvey, P. M., Kessler, J. E., Koerner, D. W., Lee, C. W., Mundy, L. G., Myers, P. C., Padgett, D. L., Pontoppidan, K., Sargent, A. I., Stapelfeldt, K. R., van Dishoeck, E. F., Young, C. H., & Young, K. E. 2003, *PASP*, 115, 965
- Fernandez, M., Ortiz, E., Eiroa, C., & Miranda, L. F. 1995, *A&AS*, 114, 439
- Finkenzeller, U. & Mundt, R. 1984, *A&AS*, 55, 109
- Gail, H.-P. 1998, *A&A*, 332, 1099
- Gauvin, L. S. & Strom, K. M. 1992, *ApJ*, 385, 217
- Gomez de Castro, A. I. 1997, *A&A*, 323, 541
- Gregorio-Hetem, J. & Hetem, A. 2002, *MNRAS*, 336, 197
- Gregorio-Hetem, J., Lepine, J. R. D., Quast, G. R., Torres, C. A. O., & de La Reza, R. 1992, *AJ*, 103, 549
- Grossman, L. 1972, *GeCoA*, 38, 47
- Hartigan, P. 1993, *AJ*, 105, 1511
- Hartigan, P., Strom, K. M., & Strom, S. E. 1994, *ApJ*, 427, 961
- Hartmann, L., Calvet, N., Gullbring, E., & D'Alessio, P. 1998, *ApJ*, 495, 385
- Henning, T., Il'In, V. B., Krivova, N. A., Michel, B., & Voshchinnikov, N. V. 1999, *A&AS*, 136, 405
- Herbig, G. H. & Bell, K. R. 1988, *Catalog of emission line stars of the orion population : 3 : 1988* (Lick Observatory Bulletin, Santa Cruz: Lick Observatory)
- Heyer, M. H. & Graham, J. A. 1989, *PASP*, 101, 816
- Higdon, S. J. U., Devost, D., Higdon, J. L., Brandl, B. R., Houck, J. R., Hall, P., Barry, D., Charmandaris, V., Smith, J. D. T., Sloan, G. C., & Green, J. 2004, *PASP*, 116, 975
- Hillenbrand, L. A. & White, R. J. 2004, *ApJ*, 604, 741
- Honda, M., Katata, H., Okamoto, Y. K., Miyata, T., Yamashita, T., Sako, S., Takubo, S., & Onaka, T. 2003, *ApJ*, 585, L59
- Houk, N. 1982, in *Michigan Spectral Survey*, Ann Arbor, Dep. Astron., Univ. Michigan, 3 (1982)
- Hughes, J. & Hartigan, P. 1992, *AJ*, 104, 680
- Hughes, J., Hartigan, P., Krautter, J., & Kelemen, J. 1994, *AJ*, 108, 1071
- Jäger, C., Molster, F. J., Dorschner, J., Henning, T., Mutschke, H., & Waters, L. B. F. M. 1998, *A&A*, 339, 904
- Kemper, F., Vriend, W. J., & Tielens, A. G. G. M. 2004, *ApJ*, 609, 826
- Kenyon, S. J., Brown, D. I., Tout, C. A., & Berlind, P. 1998, *AJ*, 115, 2491
- Kessler-Silacci, J. E., Hillenbrand, L. A., Blake, G. A., & Meyer, M. R. 2005, *ApJ*, 622, 404
- Knacke, R. F., Fajardo-Acosta, S. B., Telesco, C. M., Hackwell, J. A., Lynch, D. K., & Russell, R. W. 1993, *ApJ*, 418, 440
- Lahuis, F. & Boogert, A. 2003, in *SFChem 2002: Chemistry as a Diagnostic of Star Formation*, proceedings of a conference held August 21-23, 2002 at University of Waterloo, Waterloo, Ontario, Canada N2L 3G1. Edited by Charles L. Curry and Michel Fich. NRC Press, Ottawa, Canada, 2003, p. 335., 335
- Lawson, W. A., Feigelson, E. D., & Huenemoerder, D. P. 1996, *MNRAS*, 280, 1071
- Levreault, R. M. 1988, *ApJ*, 330, 897
- Luhman, K. L. & Rieke, G. H. 1999, *ApJ*, 525, 440
- Martin, E. L., Montmerle, T., Gregorio-Hetem, J., & Casanova, S. 1998, *MNRAS*, 300, 733
- Maxwell Garnett, J. C. 1904, *Royal Society of London Philosophical Transactions Series A*, 203, 385
- Meeus, G., Waters, L. B. F. M., Bouwman, J., van den Ancker, M. E., Waelkens, C., & Malfait, K. 2001, *A&A*, 365, 476
- Mie, G. 1908, *Ann. Phys.*, 25, 377
- Min, M., Hovenier, J. W., & de Koter, A. 2003, *A&A*, 404, 35
- . 2005, *A&A*, 432, 909
- Miroshnichenko, A. S., Mulliss, C. L., Bjorkman, K. S., Morrison, N. D., Kuratov, K. S., & Wisniewski, J. P. 1999, *MNRAS*, 302, 612
- Molster, F. J. & Waters, L. B. F. M. 2003, *LNP Vol. 609: Astromineralogy*. Edited by T. K. Henning., 609, 121
- Natta, A., Grinin, V. P., Mannings, V., & Ungerechts, H. 1997, *ApJ*, 491, 885
- Pollack, J. B. 1984, *Ann.Rev.Astron.Astrophys.*, 22, 389
- Pollack, J. B., Hollenbach, D., Beckwith, S., Simonelli, D. P., Roush, T., & Fong, W. 1994, *ApJ*, 421, 615
- Poncet, A., Montes, D., Fernandez-Figueroa, M. J., & Miranda, L. F. 1998, in *ASP Conf. Ser. 154: Cool Stars, Stellar Systems, and the Sun, 1772*
- Prato, L., Greene, T. P., & Simon, M. 2003, *ApJ*, 584, 853
- Press, W. H., Teukolsky, S. A., Vetterling, W. T., & Flannery, B. P. 1992, *Numerical recipes in FORTRAN. The art of scientific computing* (Cambridge: University Press, —c1992, 2nd ed.)
- Przygodda, F., van Boekel, R., Abraham, P., Melnikov, S. Y., Waters, L. B. F. M., & Leinert, C. 2003, *A&A*, 412, L43
- Reipurth, B., Pedrosa, A., & Lago, M. T. V. T. 1996, *A&AS*, 120, 229
- Reipurth, B. & Pettersson, B. 1993, *A&A*, 267, 439
- Rydgren, A. E. 1980, *AJ*, 85, 438
- Saffe, C., Randich, S., Mardones, D., Caselli, P., Persi, P., & Racca, G. 2003, *A&A*, 409, 993
- Sahu, M. & Sahu, K. C. 1992, *A&A*, 259, 265
- Sartori, M. J., Lépine, J. R. D., & Dias, W. S. 2003, *A&A*, 404, 913
- Servino & Piriou. 1973, *Phys.Stat.Sol.B*, 55, 677
- Sitko, M. L., Grady, C. A., Lynch, D. K., Russell, R. W., & Hanner, M. S. 1999, *ApJ*, 510, 408
- Strom, K. M., Strom, S. E., Edwards, S., Cabrit, S., & Skrutskie, M. F. 1989, *AJ*, 97, 1451
- The, P. S., de Winter, D., & Perez, M. R. 1994, *A&AS*, 104, 315
- Thi, W. F., van Dishoeck, E. F., Blake, G. A., van Zadelhoff, G. J., Horn, J., Becklin, E. E., Mannings, V., Sargent, A. I., van den Ancker, M. E., Natta, A., & Kessler, J. 2001, *ApJ*, 561, 1074
- Toon, O. B. & Ackerman, T. P. 1981, *Appl. Opt.*, 20, 3657
- Torres, G., Guenther, E. W., Marschall, L. A., Neuhäuser, R., Latham, D. W., & Stefanik, R. P. 2003, *AJ*, 125, 825
- van Boekel, R., Min, M., Waters, L. B. F. M., de Koter, A., Dominik, C., van den Ancker, M. E., & Bouwman, J. 2005, *A&A*, 437, 189
- van Boekel, R., Waters, L. B. F. M., Dominik, C., Bouwman, J., de Koter, A., Dullemond, C. P., & Paresce, F. 2003, *A&A*, 400, L21
- van den Ancker, M. E., de Winter, D., & Tjin A Djie, H. R. E. 1998, *A&A*, 330, 145
- van den Ancker, M. E., The, P. S., Tjin A Djie, H. R. E., Catala, C., de Winter, D., Blondel, P. F. C., & Waters, L. B. F. M. 1997, *A&A*, 324, L33
- van Dishoeck, E. F. 2004, *ARA&A*, 42, 119
- Waelkens, C., Waters, L. B. F. M., de Graauw, M. S., Huygen, E., Malfait, K., Plets, H., Vandenbussche, B., Beintema, D. A., Boxhoorn, D. R., Habing, H. J., Heras, A. M., Kester, D. J. M., Lahuis, F., Morris, P. W., Roelfsema, P. R., Salama, A., Siebenmorgen, R., Trams, N. R., van der Blik, N. R., Valentijn, E. A., & Wesselius, P. R. 1996, *A&A*, 315, L245
- Webb, R. A., Zuckerman, B., Platais, I., Patience, J., White, R. J., Schwartz, M. J., & McCarthy, C. 1999, *ApJ*, 512, L63
- Wooden, D. H. 2002, *Earth Moon and Planets*, 89, 247
- Zubko, V. G., Mennella, V., Colangeli, L., & Bussoletti, E. 1996, *MNRAS*, 282, 1321